UCLouvain

École polytechnique de Louvain

Exploring the Computational and Clinical Added-value of Probabilistic Optimization in Proton Therapy

Authors: **Eliot Peeters, Romain Schyns**
Supervisors: **Pr. John A. Lee, Pr. Edmond Sterpin**
Readers: **Dr. Ana M. Barragan Montero, Dr. Sophie Wuyckens, Pr. Guillaume Janssens**
Academic year 2023–2024
Master [120] in Biomedical Engineering

Abstract

The definition of the clinical target volume can be considered as a binary mask. However, the further a point is from the gross target volume, the less probability it has of being tumorous. The probabilistic definition of the clinical target volume, called the clinical target distribution, is an effective alternative to adapt the dose distribution to the probability of tumor presence. This probabilistic definition allows one to maintain tumor control probability while reducing the dose delivered to the organs at risk. Modeling the cellular surviving fraction after irradiation can also be translated into cost functions for optimizations, yet studies so far that combine radiobiological cost functions and probabilistic definition of target volumes have been limited to radiobiological effects in the target. The spatial dependence of radiobiological optimization models makes them an excellent candidate for proton pencil beam scanning.
In this Master thesis, we have developed a complete probabilistic radiobiological optimization framework for the target and organs at risk for proton pencil beam scanning. We have proven by the use of a head and neck clinical case that probabilistic radiobiological optimization allows for a decrease in the probability of normal tissue complications while maintaining tumor control probability comparable to classical dose-constrained radiobiological optimization methods.

Acknowledgment

This master thesis would not have been possible without the opportunity that has been offered to us of working for the OpenTPS project since July 2023 at the Molecular Imaging, Radiotherapy and Oncology (MIRO) laboratory of UCLouvain. We are deeply grateful for the chance that we have had to write this master thesis on a topic related to proton therapy. Therefore, we express our deep gratitude to our supervisors Pr. John Aldo Lee and Pr. Edmond Sterpin, without whom this master thesis would not have been possible and for their time and guidance throughout this academic year.

We would also like to thank the whole MIRO team for having answered our question during this project, especially Dr. Sophie Wuyckens for her advice regarding optimization, and Benjamin Roberfroid for answering all our on-the-fly questions. We are also thankful of the time taken by Dr. Gregory Buti and Luciano Rivetti in conference calls to launch us on the subject.
We are thankful to Colin Gaban for rereading our manuscript.

We would like to address our deepest gratitude to Dr. Ana Maria Barragan Montero for her follow-up on our daily work, and her always positive attitude.

Finally, We thank our friends and families for their constant support.

To all of you, thank you !
Eliot Peeters and Romain Schyns

Contents

List of Figures

List of Tables

Chapter 1

Introduction

In 2018, cancer represented 9.6 million deaths worldwide for 18.1 million diagnoses [5]. In Belgium, cancer is the first cause of premature death in 2016 [5]. In 2017, more 50% cancer patients were treated with radiation therapy, making it the main treatment used to fight tumors [6].

Although its not so recent introduction and its now well-established clinical benefits, proton therapy is used only in 1% of radiation therapy treatments (2022) [7], leaving the research field of proton therapy vast. Every treatment, whether it is conventional radiation therapy or proton therapy, undergoes a planning phase [8]. During this phase, treatment is optimized by translating clinical objectives into arbitrary cost functions [9].

The cellular effects of radiation can be modeled by the linear quadratic surviving fraction [10]. This formula has allowed the development of models for the probability of tumor control and the probability of normal tissue complications [11, 12]. Those models are inherently non-convex, taking their logarithm allows rendering them convex [13]. Despite the convexity of their logarithmic form, few attempts have been made to use these radiobiological models only for optimization [14].

Until recently, the anatomical volumes chosen for optimization were represented by 3D binary masks [15]. However, in 2018 the concept of probabilistic volumes [16] was introduced, resulting in new definitions of cost functions and probability of tumor eradication. The volume of greatest interest in this master thesis is the clinical target volume and its probabilistic counterpart, the clinical target distribution.

To the best of our knowledge, there is only one study by Bortfeld *et. al.* [17] in which the combination of clinical target distribution and tumor control probability has been investigated to develop a radiobiological cost function for optimization. However, the optimization framework of this study still relied on a radiation dose prescription to the target and was limited to the study of tumor control only, excluding the organs at risk. Prospects of probabilistic definitions of the clinical target volume combined with an optimization framework based on the tumor control probability and normal tissue complication probability without any prior dose prescription are yet to be explored.

The purpose of this master thesis is to study the computational feasibility of a cost function based on tumor control and normal tissue complications for probabilistic definition of the clinical target volume. Once the model has been developed, the clinical added value of this new optimization method will be evaluated against the non-probabilistic and conventional methods.

We will make our way through this subject by first motivating the use of radiation therapy and proton therapy, then going over the course of a proton therapy treatment, and finish by describing the probabilistic and biological model and how to unify them. The results will be presented on the clinical case of a patient with a head and neck tumor.

Throughout this master thesis, we have tried to remain as intelligible as possible for the covered concepts by providing plain illustration and striving to bring enriching illustrations.

Chapter 2

Radiation Therapy

2.1 A short history of radiation therapy

2.1.1 Discovery of radiations

X-rays were discovered by William Roentgen in 1895 and not long afterwards, in May 1896, the toxicity of radiation became apparent with consequences such as hair loss through experiments performed by Leopold Freund [18]. This toxicity of radiation led to the idea of using it to kill cancerous cells. Thus, in July 1896, Victor Despeignes treated the first patient (stomach cancer, bifractionated treatment) with radiation therapy [18]. Until 1920, radiations were not used systematically for tumor treatment, but by a few doctors who believed in the effect of radiation. Due to the low-energy X-rays produced at that time, treatments were only able to penetrate the surface of the skin [18].

2.1.2 Higher energies

As it became clear that higher-energy X-rays were needed to treat deeper tumors [18], Henri Coutard and Claudius Regaud from Institut Curie discovered between the 1920s and 1930s that hypofractionation of treatment would lead to severe tissue reaction and were the first to propose treatments over several weeks [19, 20]. The invention of the Coolidge tube allowed deeper tumors to be irradiated with energies ranging from 180 to 200 kV [20], and between the 1920s and 1950s, the focus was on improving the energy of the radiation delivered [20]. In 1930 Ernest Lawrence and Milton Livingstone invented the cyclotron [20], a major milestone in the development of proton therapy, but we will come back to it later. Between 1950 and 1985, radiotherapy facilities were capable of producing beams with megavoltage energy orders with linear electron accelerators (linacs) with energies ranging from

4 to 20 MeV and cobalt radiotherapy units with energies of 1.3 MV [20].

In 1982 the Swedish medical physicist, Anders Brahme introduced in his paper "Solution of an integral equation encountered in rotation therapy" [21] intensity modulated radiation therapy (IMRT) [19]. Brahme proposed a new type of dose profile with a photon beam shaped by a nonlinear wedge-shaped filter [21]. His conclusions were that such types of filters could improve dose uniformity in the target with rotation around it (even if the target is slightly off-centered with the rotation) [21]. This work led the way for dose shaping and in 1992 the first IMRT machine with multileaf collimator (MLC), the NOMOS MIMIC (Figures B.1 and B.2) system that could be attached to linacs, was introduced on the market [19].

Although IMRT was not used in clinical practice until 2000 [19], it is now the standard when it comes to radiation therapy. The early 2000s are also the years of the rise of the C-type Linacs and Tomotherapy [19].

2.1.3 Treatment planning systems

Regarding treatment planning, we must consider that computed tomography (CT) scans were not implemented as today for radiation therapy [19]. Modern 3D treatment planning emerged in 1994 after the combined efforts of different working groups [22]. However, the first study to implement 3D treatment planning dates back to 1973, when researchers used computed animated films to plot isodose lines on it (Figure B.3) [23]. Today, treatment planning systems (TPS) using 3D treatment planning are fully implemented in clinical practice [8].

2.1.4 Ion beam therapy

The first proposal to use accelerated protons as particles for radiation therapy was written in 1946 by Robert R. Wilson [20]. Inspired by the invention of the cyclotron by Lawrence and Linvingstone, Wilson proposed that due to the so-called Bragg peak (*i. e.* the localized deposition of the protons energy, more on this in Section 2.4), protons could be used to irradiate tumors while sparing healthy tissues (Figure 2.1) [24]. The first clinical use of protons occurred at Berkley in 1954 and the opening of the first proton therapy (PT) facility in 1990 at the Loma Linda University Medical Center [20]. Since then, more and more PT facilities have emerged around the world and have made PT a serious alternative to regular IMRT with improved healthy tissues sparing (Figure 2.2).

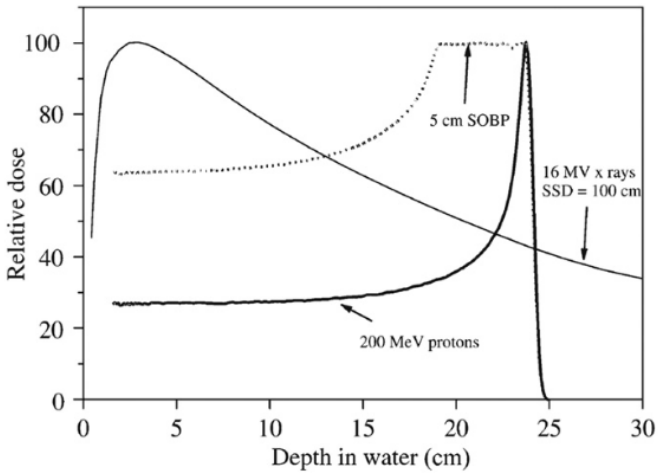

Figure 2.1: Depth-dose curve of proton and photon (each normalized at 100 for the highest dose) [25].

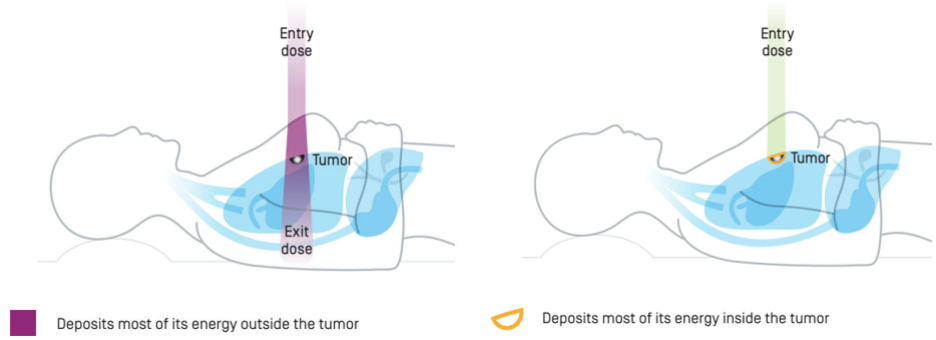

Figure 2.2: IMPT on the left and IMRT on the right [26]. We can clearly see healthy tissues are less irradiated with protons

2.2 Radiobiology

Radiobiology is the study of the effect of radiation on living cells and tissue [10], thereby it is an essential tool to understand radiation therapy. Radiation exposure is quantified by the absorbed dose [10], and the absorbed dose is defined as [27] :

$$D = \frac{d\bar{\epsilon}}{dm} \ , \tag{2.1}$$

$$\bar{\epsilon} = R_{in} - R_{out} + \Sigma Q \ , \tag{2.2}$$

with $\bar{\epsilon}$ the mean imparted energy in the volume of mass m. The mean energy imparted is equal to the equation 2.2 in which R_{in} is the mean total radiant energy

of the ionizing particles entering the same volume of mass m, R_{out} is the mean total radiant energy of the particles leaving the volume and ΣQ is the mean total decrease in rest energy [27]. Since the computation of the mean imparted energy changes for the uncharged and charged particles, the latter will be further discussed in section 2.4.1.

Ionizing radiation passes through materials and is only stopped because of absorption. In cells, this absorption can lead to the breakdown of molecular bonds, which are of particular interest when it comes to DNA [10]. When radiation damages DNA, either the generated modification has no effect on the function, either it has effect but the cell can repair it, or, lastly, the cell cannot repair the damage done to the DNA [10]. When radiation passes through the cell, DNA damage can be done directly or indirectly (Figure 2.3) by ionizing water molecules (the human body is made up of approximately 70% water) [10].

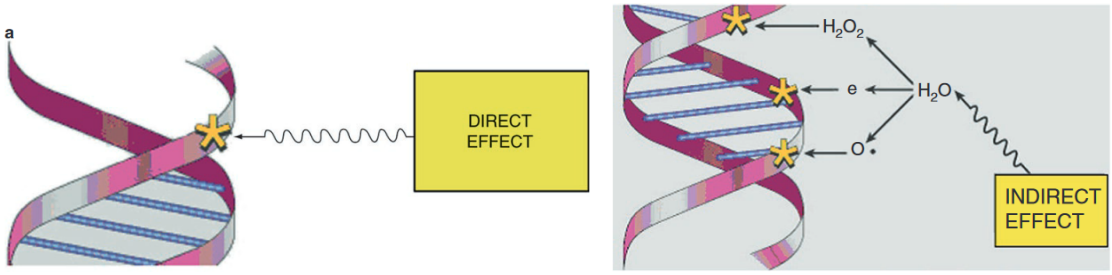

Figure 2.3: Direct and indirect effects of radiations on DNA [10]

If damage to cell DNA is too extensive and cannot be repaired, it leads to cell apoptosis (death) [10]. Among the multiple unique features of cancer cells, one that is convenient for radiation therapy is their genetic instability, which means that they cannot repair DNA defects as non-tumorous cells [10]. The surviving fraction (SF) of cells exposed to radiation can be modeled with the linear quadratic (LQ) Poisson model defined as [13, 28, 10] :

$$SF(D) = e^{-\alpha D - \beta D^2/n} \quad . \tag{2.3}$$

In this model, α $[Gy^{-1}]$ (also known as radiosensitivity) represents damages in DNA that cannot be repaired (single-track into the chromosome) and β $[Gy^{-2}]$ represents the damages that can be repaired by the cell (double track) and D is the total dose in $[Gy]$, n the number of treatment fractions (Figure 2.4 and 2.5). The number of fractions is the number of times the total dose is divided to be given daily. The ratio α/β will define whether the cell is an early responding cell or a late responding cell (Figure 2.6) [10].

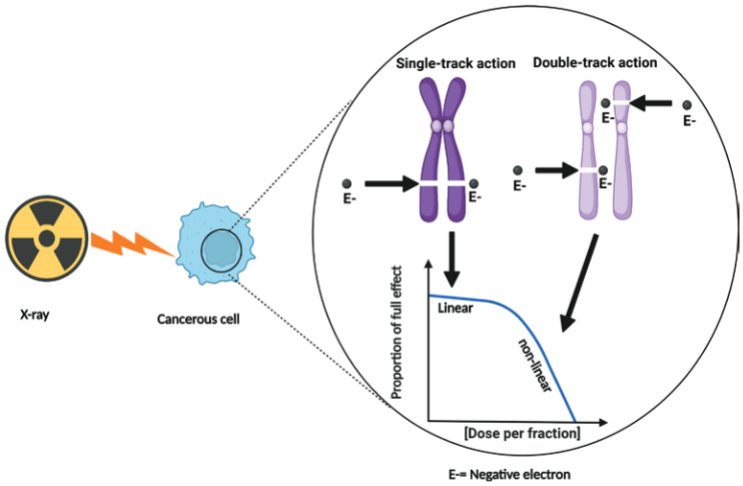

Figure 2.4: The SF of cells depending on the type of track action. The linear part of the curve is due to α and the non-linear to β [28].

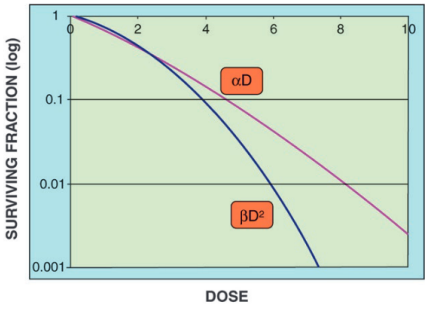

Figure 2.5: Influence of the α and β parameters on the surviving fraction [10].

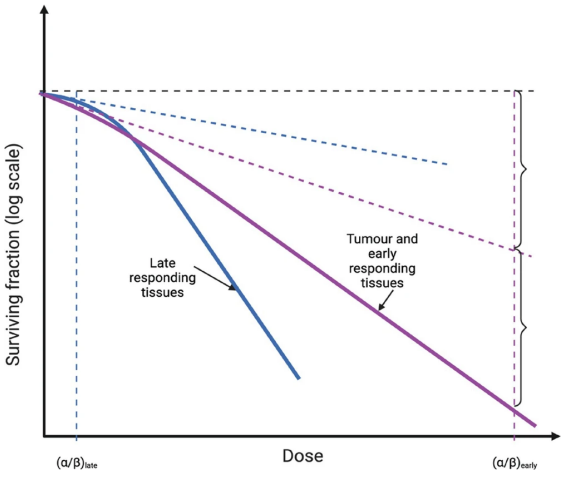

Figure 2.6: Late and early responding cells $\alpha/\beta_{late} < \alpha/\beta_{early}$ the brackets is when the αD kills the βD^2 term [29].

2.3 The paradigm of radiation therapy

Simply basing our explanation on the SF_{LQ} model 2.3 (and without going too much into detail like reoxygenation of tumor cells [28]), radiation therapy is based on a fundamental property of tumors and healthy tissue [28] :

$$\frac{\alpha}{\beta}_{tumors} (\approx 10Gy) > \frac{\alpha}{\beta}_{normal\ tissue} (\approx 3Gy) \ . \tag{2.4}$$

It is possible to use the shoulder effect of the late responding cells (Figure 2.6) [10] by fractionating the treatment dose received by the patient. The fractionation of treatments allows normal tissue cells to repair damages done to DNA that they are able to repair (known as sublethal damages, SLDs) [28]. Thus, treatment if fractionated into smaller daily doses of the total dose (generally 2Gy/day for 30 days) [28]. It is important to note that the treatment fraction should be separated by a minimum of 8 hours to allow cells to repair SLDs [28]. SF_{LQ} curves can be adapted to treatment fractionation (Figure 2.7), we can see that more fractions allow for a higher dose for the same cell survival.

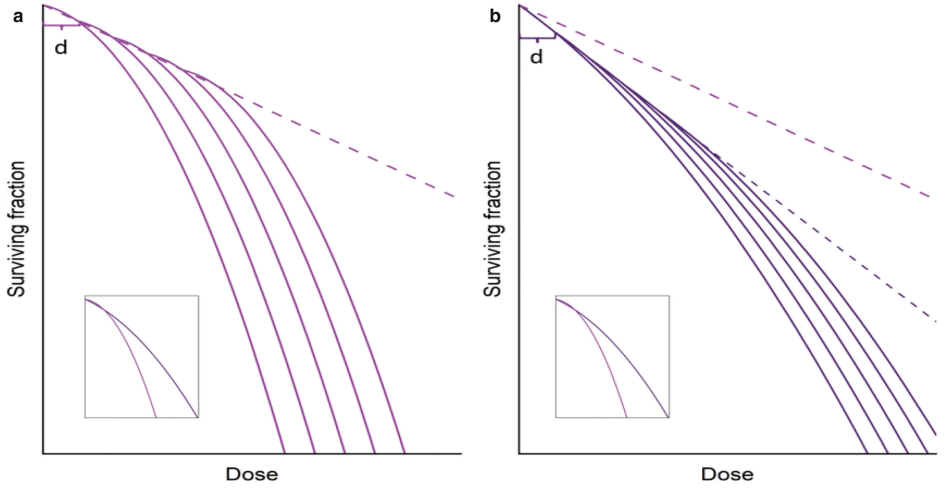

Figure 2.7: Fractionation of treatment and cells survival for late responding cells (a) and early responding cells (b) [29].

When planning a treatment, we need to balance the tumor control probability (TCP) and the normal tissue complication probability (NTCP) [28]. Both are directly related to the survival probability of normal or tumor cells (models explained in Section 3.4.1). In between the two curves lies the optimal treatment. The distance between the two curves is known as the therapeutic index or window [28, 10] (Figure 2.8).

As mentioned before, fractionation of the treatment enlarges the therapeutic window (Figure B.4) as well as improve the TCP. We can also define the probability of uncomplicated treatment [28] or probability of undamaged cure [10] which is the probability of having the optimal treatment (UTCP) depending on TCP and NTCP. The optimal treatment probability is also increased with fractionation of treatments (Figure 2.9).

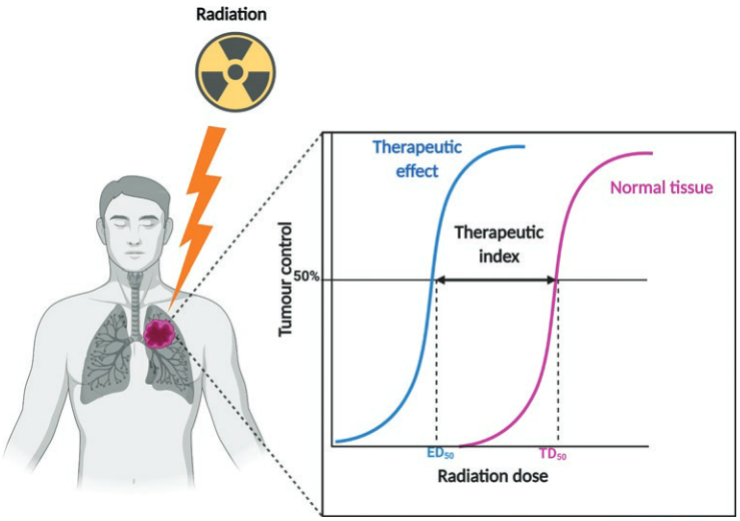

Figure 2.8: TCP and NTCP curves in function of radiation dose [28]. The D_{50} are known as the dose at which 50% of the cells dies.

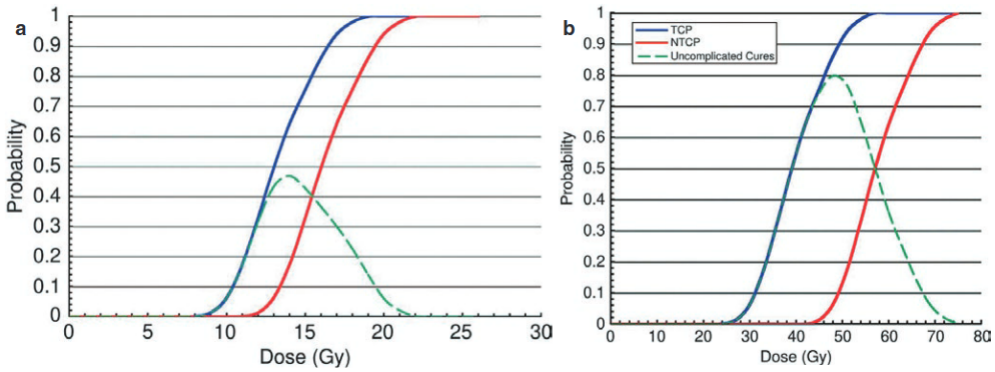

Figure 2.9: Probability of uncomplicated treatment for a single dose (a) and a fractionated dose (b) [28].

2.4 Proton therapy

2.4.1 Physics of proton therapy

To compute the dose deposited by proton through matter, we need to introduce the concept of stopping power. This quantity is defined as the energy lost dE by a particle traveling through a distance ds of matter [27].

For ease of use, we will define the mass stopping power as the stopping power divided by the volume mass ρ :

$$\frac{S}{\rho} = \frac{1}{\rho}(S_{el} + S_{rad}) = \frac{1}{\rho}\left(\frac{-dE}{ds}\right) \quad . \tag{2.5}$$

For protons, this stopping power is of the order of 260.8 MeV cm^2/g for a 1 MeV beam thought water [30]. We notice that there is a radiative component (S_{rad}) and an electronic component (S_{el}) to the stopping power, for proton therapy the radiative component is negligible [31]. The stopping power of protons can be approximated with the Bethe-Bloch formula (simplified version) [27] :

$$\frac{1}{\rho}S_{el} \propto \frac{Z}{A}\frac{z^2}{\beta^2}[f(\beta) - lnI - \frac{C(\beta)}{Z} - \delta(\beta)] \quad . \tag{2.6}$$

With Z and A the atomic number and mass of the medium, z the atomic number of the projectile, β the relativistic factor of the projectile and I, the mean excitation energy. Stopping power for compounds can be computed vie the Bragg additive rule which states that stopping powers can be weighted in terms of fractional weight of an element in a compound and added [27].

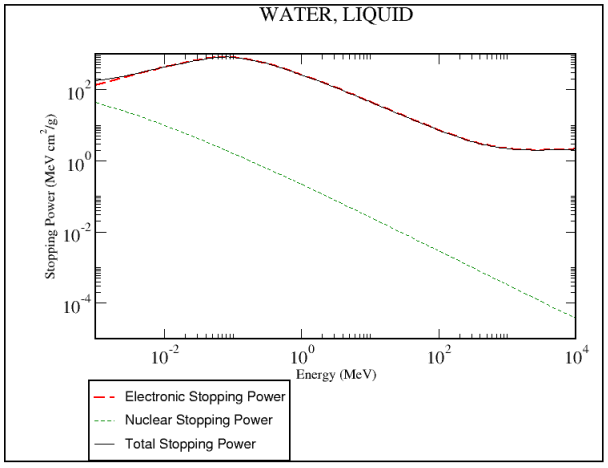

Figure 2.10: Stopping power of water in function of the energy [30].

The fact that the stopping power increases as the energy decreases in equation 2.6 ($S_{el} \propto \frac{1}{\beta^2}$) is the cause of the Bragg peak (Figure 2.1). Knowing the stopping power and inferring the continuous slow down approximation (CSDA, which states that protons lose energy in a continuous way), we can compute the range of protons

through a medium with the following [27, 31] :

$$R_{CSDA} = \int_0^{E_0} S_{el}(E)^{-1} dE \ . \tag{2.7}$$

When going through matter, protons suffer three types of energy losses [31]:

- Inelastic Coulomb interaction with atomic electrons (Figure 2.11 (a)) that will be the main component of the stopping power and might generate secondary electrons (but of small range).
- Elastic Coulomb scattering with nuclei (Figure 2.11 (b)) that will deviate protons and thereby broaden the beam and decrease the range
- Interaction with atom nucleus and formation of secondary particles (Figure 2.11 (c)) that will generate secondary particles.

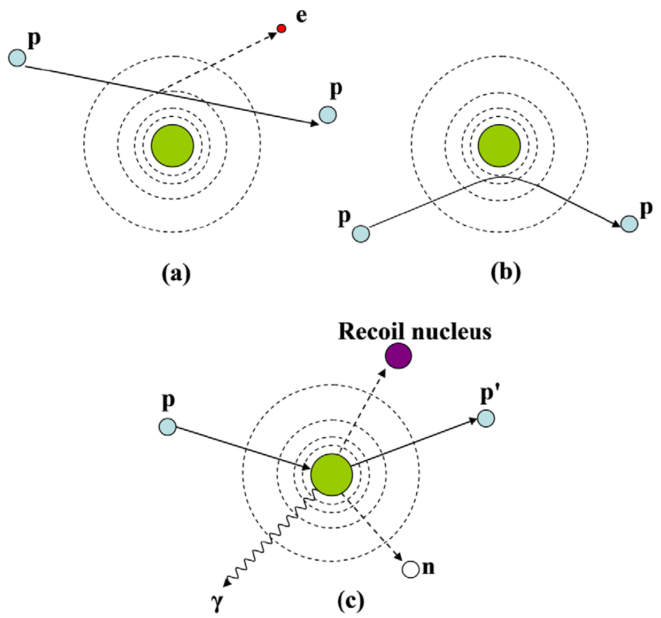

Figure 2.11: Interactions of protons in matter [31]

Because in proton therapy we are interested in the dose in small volume (voxels), we can infer *restricted charged-particle equilibrium* (RCPE). It states that for small volumes, for particles with small ranges, each particle leaving the volume will be replaced by another of the same energy in terms of expectation values [27].

This allows us to derive (recalling equation 2.1) the dose delivered by protons in a medium depending on their stopping power [27]:

$$D_{med} \overset{\text{RCPE}}{=} \phi_{med}[\frac{S_{el}(E)}{\rho}]_{med} \ , \tag{2.8}$$

with ϕ the proton fluence in an area da:

$$\phi_{med} = \frac{dN}{da} \ . \tag{2.9}$$

And because the energy of protons follows a gamma distribution (this is called energy straggling) [31] we arrive at the finale equation for the dose of a poly-energetic beam [27]:

$$D_{med} \overset{\text{RCPE}}{=} \int_0^{E_{max}} [\phi_E]_{med}[\frac{S_{el}}{\rho}]_{med} dE \ . \tag{2.10}$$

Finally, we have to consider that for the same absorbed dose, the effects of radiations are not the same on tissues. Protons are low-LET (linear energy transfer) particles. What this means is that the ionization of atoms along the proton tracks is more clustered [32] (Figure 2.12). One effect of those low-LET tracks is that there is more ionization in the chromatin fibers that compose DNA [33] (Figure 2.13). LET has been defined by ICRU as the energy deposited by a particle locally along its trajectory, ignoring the kinetic energy of the secondary electrons produced [27].

Having the LET of protons in mind, we can now define the Radiobiological effectiveness (RBE) as the relative biological effectiveness between some type of radiation and the reference of 250kV X-rays or ^{60}Co gamma rays [34]. The RBE of protons is due to several factors, including the LET and a value of 1.1 has been commonly adopted [32].

2.4.2 Proton therapy simulation

Proton beams through tissues can be modeled using pencil-beam (PB) algorithms or Monte Carlo (MC) simulations [35]. Pencil-beam algorithms being faster, they were the preferred choice during early developments of simulations. However, due to some inaccuracy of PB algorithms with heterogeneities and recent augmentations in computing capabilities, MC simulations are now the standard when it comes to proton therapy simulations [35, 36].

MC simulations are intrinsic statistical and random methods. In MC simulations, particles are simulated individually and their path is simulated by the following [36]:

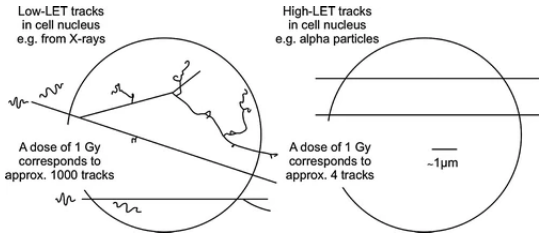

Figure 2.12: Ionization along a low- and high-LET track [32].

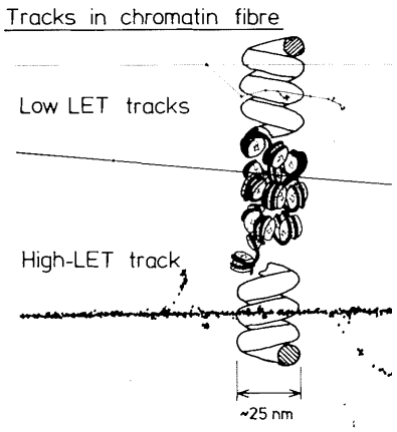

Figure 2.13: Low- and high-LET tracks in chromatin [33]. (Dimensions of the track and DNA have been modified for the figure.)

- Random selection of the distance until next "hard" interaction
- Transport of the particle to the site of interaction (including geometrical factors)
- Random selection of the interaction that will occur
- Simulation of the interaction
- Repeat until full absorption of the particle and the secondary particles generated.

The stopping powers needed to compute the particle path are extracted from CT calibration [36]. Those calibrations were derived from data linking HU units and tissue density / material [36]. It should be noted that PB algorithms use water equivalent to compute the dose and thereby produce a D_w image, while MC simulations directly output a dose to medium D_{med} [36]. The D_{med} gives more insight into the dose distribution and the conversion from D_{med} to D_w should be avoided due to several discrepancies [37]. Finally, the dose is scaled with the RBE (discussed above) [36].

2.4.3 The course of a proton therapy treatment

The steps of a proton therapy treatment are similar to those of an IMRT treatment. Those steps are the following [38] :

1. Pretreatment, TPS and machine quality assurance (QA) : the calibration of the CT for HU density conversion data is done through shooting into a water phantom.

2. Imaging of the patient and organ segmentation: CT (or other modalities) is used to delineate organs and tumors. The delineation of the tumor will be discussed in Section 2.5.

3. Planning and optimization : once the target is defined, the plan is optimized to spare as much healthy organs as possible. The plan is then reviewed to ensure that it meets the imposed criteria.

4. Positioning of the patient: the patient is placed on the treatment couch using kV CT and markings.

5. Delivery of treatment.

6. Daily imaging to infer tumor changes: to assess tumor shrinkage and avoid range errors, the patient is imaged in between treatment fractions to change the plan if necessary.

7. Return to Step 4.

2.4.4 Proton therapy facility

Proton facilities are complex systems and thereby need to be designed carefully due to the place that the equipment occupies. A proton therapy delivery system is made up of three main parts [39] :

- The accelerator: raises the energy of protons to the desired or sufficient level.
- The beam transportation and energy selection: transport the beam to the treatment room and discriminate protons with incorrect energy.
- The delivery system: composed of the gantry, the nozzle, the snout, and the patient positioning system.

There exist several different delivery technologies and gantries, but we will focus here on the facility of the UZ Leuven Particle Center. Particle center uses two IBA ProteusONE systems, one for research and one for treatment [40]. The IBA ProteusONE system is a pencil beam scanning (PBS) system coupled to a cyclotron [41, 39]. The nozzle can rotate from an angles of 0 to 220 ° around the patient (Figure B.5)[39], allowing more complicated tumors to be handled. PBS is a technique that uses two sets of dipole steering magnets to steer the proton beam

(Figure 2.14) [39]. The tumor is irradiated by a series of beamlets with different spots in the tumor [39]. Optimization is carried out by finding the best series of weights for the beamlets because of the dose being the superposition of each beamlets [39].

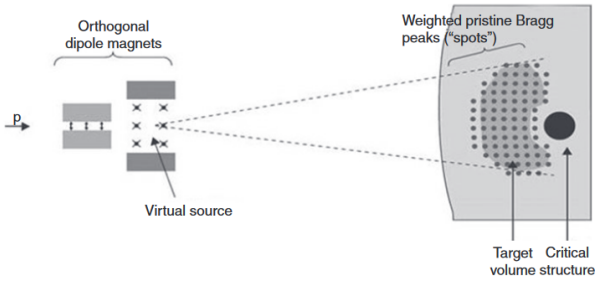

Figure 2.14: Pencil beam scanning [39]

2.5 The concept of margins

When planning a radiation therapy treatment, the patient first undergoes imaging. Multiple imaging modalities can be used for tumor identification (CT, MRI, PET/CT) [42]. After imaging, a physician delineates the volumes of the different organs in the 3D image of the patient [42]. Those volumes are separated between the organs at risk (OAR) and the targets [15].

For target delineation, we must introduce the concept of margins. The margins can be seen as the peels of an onion, each volume encompassing another (Figure 2.15). Margins were first introduced in the ICRU report 50 and are now made up of the gross target volume (GTV), the clinical target volume (CTV), the internal target volume (not described here) and the planned target volume (PTV) [15].

2.5.1 Gross target volume

The gross target volume is *the gross demonstrable extent and location of the tumor* [15]. The GTV can be thought as what we "see" or "feel" upon examination. Since functional imaging (PET) can give different GTV than structural imaging (CT, MRI) it is important to specify the imaging modality used [15]. The GTV can also be used as a marker to infer treatment regression, therefore the dose received should also be specified [15] (Figure 2.16). If the GTV is changed because of the treatment, the treatment plan should also be adapted to the new GTV [15].

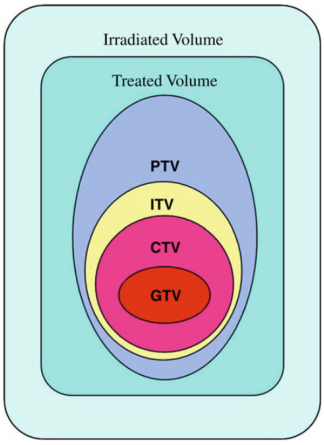

Figure 2.15: Margins of the target. [42]

As the definition of the GTV varies depending on the imaging modality, there are certain uncertainties associated with the delineation. Those uncertainties are carried out through the CTV but can be taken into account in the CTV-to-PTV margin [15].

2.5.2 Clinical target volume

The clinical target volume is *a tissue volume that contains a demonstrable GTV and/or subclinical malignant disease with a certain probability of occurrence considered relevant for therapy* [15]. So, the CTV is an extension of the GTV that contains the region where there is probably tumor infiltration, and this probability is judged relevant. Indeed, some tumor infiltration that we do not see when defining the GTV might appear [43] (Figures 2.17 and 2.18). Therefore, the definition of CTV is based on clinical judgement (whether to opt for a threshold 5% or 10%) and knowledge of the environmental anatomy [15].

2.5.3 Planned target volume

The planned target volume is *a geometric concept introduced for treatment planning and evaluation* [15]. The PTV is an extension of the CTV to ensure proper dose coverage despite the presence of geometrical uncertainties. Those uncertainties arise from tumor movement or setup errors (patient positioning) [15]. PTV can be defined through the knowledge of the impact of uncertainties.

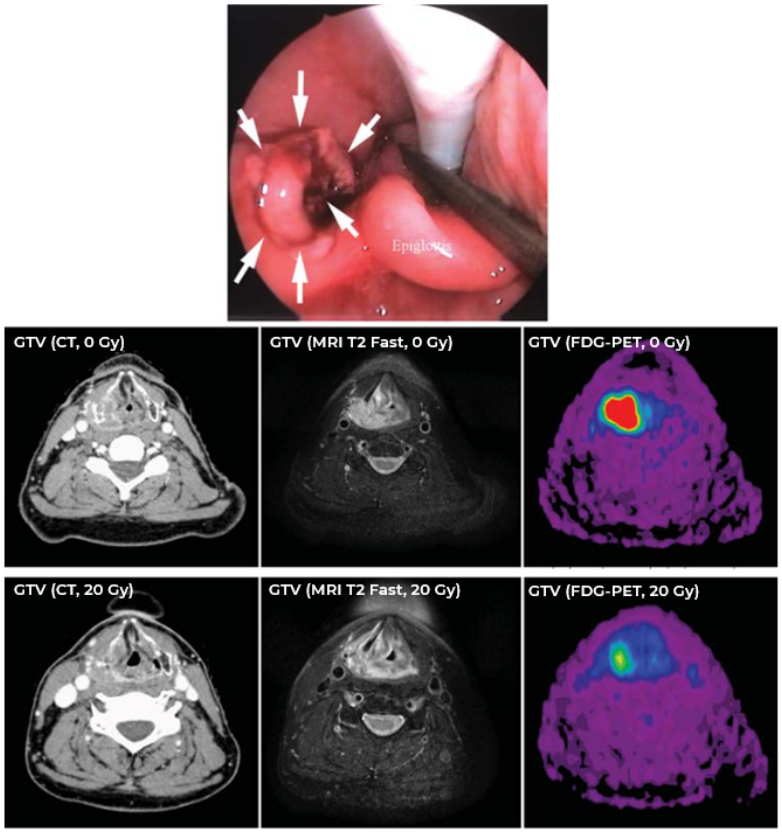

Figure 2.16: Evaluation of the GTV and evolution throughout the treatment. Modified from [15].

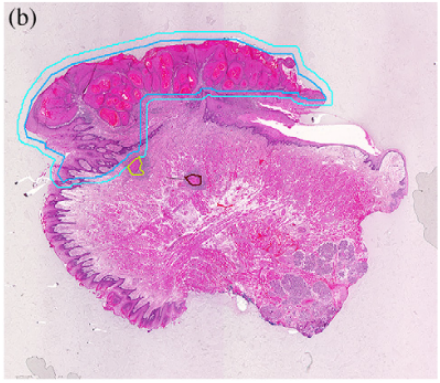

Figure 2.17: Microscopic view of GTV in blue and infiltration in yellow and red [43].

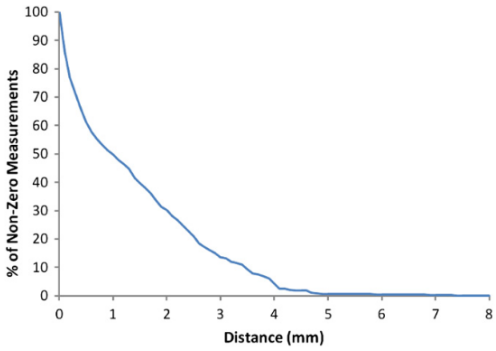

Figure 2.18: Probability of finding tumor infiltration in function of distance (10 cases, oral tong cancer) [43].

2.6 Dose volume histogram

To supplement the 2D spatial information provided by a dose image, one can make use of a dose-volume histogram (DVH). Dose-volume histogram represent the amount of dose received by a portion of the volume of any organ/target [42]. Such representations allow a comprehensive way to represent data, but should always be supplemented by a dose image [42]. The most commonly used type of DVH is cumulative DVH (cDVH), since they are the most widely used type; the "c" is far often dropped in the literature and will also be used in this work. cDVH represents the portion of a volume that receives at least a certain dose (Figure 2.19).

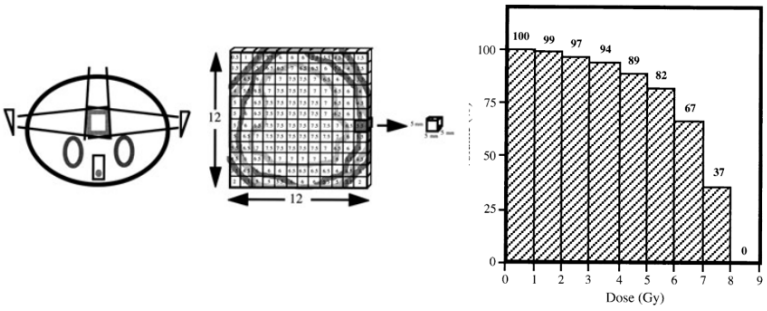

Figure 2.19: Cumulative dose volume histogram [42].

Mathematically, we can describe (c)DVH the following way [44];
Let :

$$\kappa : \mathbb{R}_0^+ \to \mathbb{N}_0, D \to \kappa(D) \ , \tag{2.11}$$

and the bins

$$\begin{aligned} k \in \mathcal{K} := \{0, ..., K\} \\ \text{s.t.} \quad \kappa(0) = 0 \\ \kappa(D_{max}) = K \ . \end{aligned} \tag{2.12}$$

Then the DVH for a volume of N elementary isotropic voxels, each receiving a dose d_i is defined by :

$$h_k = \sum_{i=1}^{N} \delta_{k,\kappa(d_i)} \ , \tag{2.13}$$

$$\mathrm{DVH}_k = \frac{100\%}{N} \sum_{j=k}^{K} h_j \ . \tag{2.14}$$

2.7 Uncertainties

Uncertainties in proton therapy can be divided in three categories [45] :

- Physical uncertainties : the proton range is inaccurate
- Geometrical uncertainties : (mostly) translation of the tumor
- Anatomical uncertainties : GTV to CTV extension and shrinkage of the tumor

2.7.1 Physical uncertainties

Physical uncertainties are uncertainties related to the calculation of the proton pathways, leading to range uncertainties [45]. They can be of multiple origins [46] :

- CT acquisition : those can originate from noise in the acquisition, grid size to large (partial volume effect), and incorrect tissue segmentation (to obtain the stopping power).

  solution : *better CT and segmentation algorithms. This is more relevant to the field of radiology*

- Conversion to Stopping powers : imprecision in the conversion from HU to density to scale the stopping power, conversion dose to water - dose to medium.

  solution : *one solution proposed by Möhler et al. [47] is to use dual-energy CT (DECT) to reduce errors in stopping power prediction*

- Dose computation : analytical algorithms for dose computation handles badly lateral heterogenities

  solution : *use MC simulations*

- Radiobiology : the RBE of protons has been assumed to be a flat 1.1. However, the LET increases with depth (which is compensated by decreasing fluence to achieve homogeneous depth dose profile), and, since the LET and the RBE are related, the RBE increases at the end of the Bragg peak (this does not affect much tissues with a high α/β ratio)

  solution : *Grassberger et al. have proposed using LET voxel map for biological optimized treatment [48, 49]*

Source	**Range uncertainty (σ)**
CT noise	$\pm 0.5\%$
CT grid size	$\pm 0.3\%$
CT segmentation	$\pm 0.5\%$
Conversion to stopping power	$\pm 1.5\%$
Analytical dose computation algorithm	$-0.7\% \rightarrow \pm 2.5\%$
MC dose computation algorithm	$\pm 0.2\%$
Radiobiology	$+0.8\%$
total excluding RBE with analytical	$2.7\% \rightarrow 4.6\% + 1.2mm$
total excluding RBE with MC	$2.4\% + 1.2mm$

Table 2.1: Table of uncertainties adapted from [46]. The $+1.2mm$ refers to uncertainties independent of dose calculation.

2.7.2 Geometrical uncertainties

Geometrical uncertainties or errors are due to translation in the location of the tumor [45]. They can be separated between systematic (preparation or setup) errors and random (execution) errors. The setup errors have the effect of shifting (Figure 2.20 (B)) the dose, they are stochastic over a population of patients [50]. Setup errors occur when planning the treatment. Random errors occur between fractions and have the effect of blurring the dose [50] (Figure 2.20 (B)).

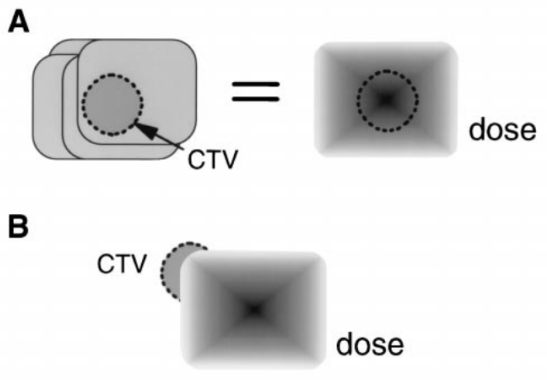

Figure 2.20: Setup and random errors effect on the dose [50]. (A) blurring of the dose between treatment fraction. (B) Shifting of the dose between patients.

If we suppose that all errors (setup and random) follow a Gaussian distribution centered at 0, we can treat errors the following way [50, 45] (Figure 2.21):

Source	**Setup**	**Random**
Tumor motion	Σ_{TM}	σ_{TM}
Baseline shift (breathing motion)	Σ_{BL}	σ_{BL}
Positioning the patient	Σ_{SETUP}	σ_{SETUP}
Delineation of the CTV	Σ_D	/
Penumbra of the beam	/	σ_p
Total setup errors	$\Sigma = \sqrt{\Sigma_{TM}^2 + \Sigma_{BL}^2 + \Sigma_{SETUP}^2 + \Sigma_D^2}$	
Total random errors	$\sigma = \sqrt{\sigma_{TM}^2 + \sigma_{BL}^2 + \sigma_{SETUP}^2 + \sigma_p^2}$	

Table 2.2: Sources of the random and the setup errors.

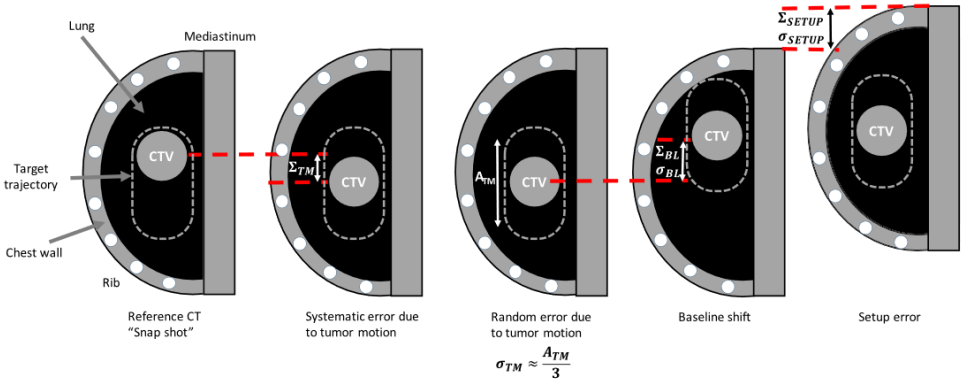

Figure 2.21: Random and setup errors in a lung phantom [45].

2.7.3 Anatomical uncertainties

Anatomical uncertainties cannot be modeled with margins. Therefore, the solution is to adapt the plan to changes in patient anatomy (Figure 2.16), it is called adaptive radiation therapy [45]. Re-planning efficiently and accurately are the research goals of adaptive radiation therapy [51]. As these strategies are relevant to other fields of radiation therapy, they will not be described here.

2.8 The Van Herk margin recipe

Now that we have defined the different target volumes and uncertainties in radiation therapy, we can extend our discussion to the recipe for the CTV-to-PTV extension. Although there are several different recipes for this extension [52], with over 1800+ citations, the Van Herk margin recipe is the most popular. This recipe has been developed by Marcel Van Herk *et al.* in his paper *"The probability of correct target dosage : Dose-population histograms for deriving treatment margins in radiotherapy"* [50]. This recipe only accounts for geometrical uncertainties. Knowing the total of setup errors (Σ) and random errors (σ) the margin formula is [50] :

$$M_{PTV} = \alpha\Sigma + \beta(\sigma - \sigma_p) \ . \tag{2.15}$$

This recipe is valid when the hypothesis is made that the dose distribution is stable, uniform, spherical, and large enough compared to the uncertainties [50, 45].

For the random errors to depend on the penumbra is difficult and must depend on the beam calibration unless the following approximation is made [50] (Figure 2.22):

$$\begin{aligned} \beta(\sigma - \sigma_p) &= \beta(\sqrt{\sigma_{TM}^2 + \sigma_{BL}^2 + \sigma_{SETUP}^2 + \sigma_p^2} - \sigma_p) \\ &\approx \gamma(\sqrt{\sigma_{TM}^2 + \sigma_{BL}^2 + \sigma_{SETUP}^2}) \\ &\approx \gamma\sigma' \ . \end{aligned} \tag{2.16}$$

Now that our equation has been laid out, we can calculate for systematic errors, the confidence interval in the population histogram (% of patient getting correct dosage) and for the random errors the dose level (% of the volume between CTV and PTV getting the correct dosage) (Table 2.3).

Thereby, if we want a dose coverage of 95% in 3D (Figure 2.23), the formula is :

$$M_{PTV} = 2.79\Sigma + 0.7\sigma' \ .$$

2.9 Conventional optimization methods

The optimization of a treatment plan depends greatly on the technique used. Since we are here using a proton PBS technique, we will describe the framework associated with this technique. Compared to other treatment delivery methods, PBS has the advantage of having a large number of degrees of freedom [9].

Confidence level (% of patients)	α		
	1D	2D	3D
80	1.28	1.79	2.16
85	1.44	1.95	2.3
90	1.64	2.15	2.50
95	1.96	2.45	2.79
99	2.60	3.04	3.36

Dose level (%)	β	γ
80	0.84	0.40
85	1.03	0.50
90	1.28	0.60
95	1.64	0.70
99	2.34	0.95

Table 2.3: Coefficients for margins adapted form [50]

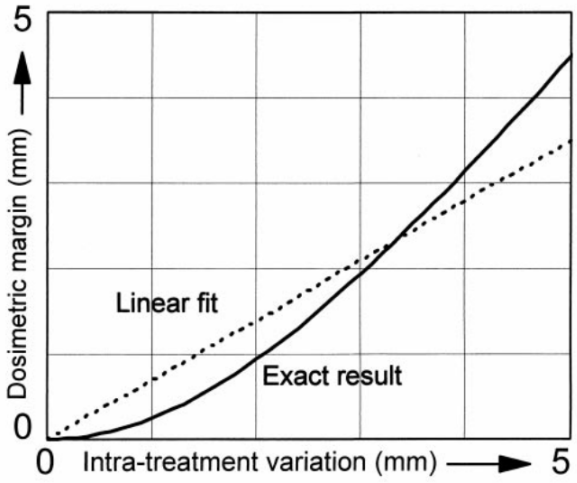

Figure 2.22: Linear approximation and quadratic result for random errors with $\sigma_p = 3.2mm$ [50].

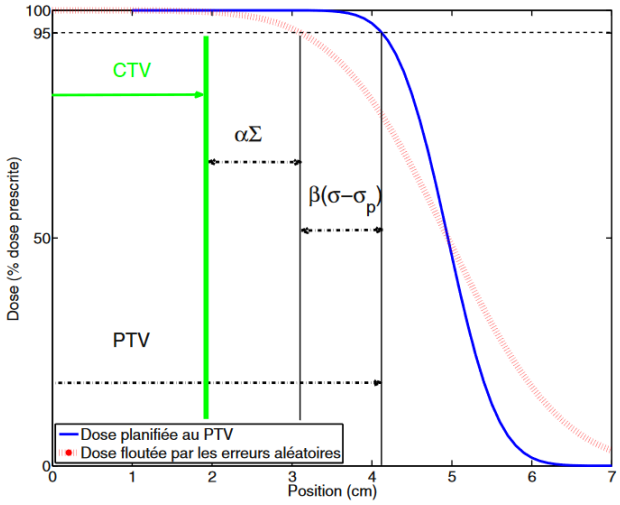

Figure 2.23: The effect of the Van Herk margin recipe on the DVH with 95% dose coverage [45].

Planning with PBS implies that every beamlet has its own position, energy, and number of protons. It is the number of protons per beamlet that is optimized and is referred to as "weight" [9]. Optimization of a plan means achieving ideal target coverage while sparing as much as possible OARs. This trade-off is quantified by a cost function to minimize, thereby the scheme [9, 53, 54] :

$$
\begin{aligned}
&\min_{\mathbf{x}}\{f(\mathcal{D})\} \\
&\quad \text{s.t.} \quad \mathcal{D} = \mathcal{B}\mathbf{x} \\
&\qquad\quad x \geq 0 \quad \forall x \in \mathbf{x} \\
&\quad \text{with} \quad \mathbf{x} \in \mathbb{R}^m, \mathcal{B} \in \mathbb{R}^{N\times m}, \mathcal{D} \in \mathbb{R}^N \\
&\qquad\quad \mathcal{D}, \in \mathbb{R}^N \leftrightarrow \mathbf{D} \in \mathbb{R}^{n_x \times n_y \times n_z} \quad ,
\end{aligned}
\tag{2.17}
$$

$\mathbf{x}$ is the beamlet weight vector for m spots, $\mathcal{A}$ is the beamlet matrix with N rows corresponding to the number of voxels in the patient ($n_x \times n_y \times n_z$ 3D CT) and m columns corresponding to the beamlets, $\mathcal{D}$ the flattened dose matrix and its associated $\mathbf{D}$ dose matrix in 3D.

Now that we have defined our variables, let us define several cost functions with their own weight (w) such that [9] :

$$
f(\mathcal{D}) = \sum_i w_i f_i(\mathcal{D}) \quad . \tag{2.18}
$$

There are several constrain possible, each associated with a cost function quadratically related to a dose prescription/limit (D_0) [9]. The most used ones are the maximum dose (equation 2.19) and minimum dose (equation 2.20) [53]. The costs are calculated over a region of interest (ROI, r) with N_r voxels. It is important to note that multiple cost functions can be associated with the same ROI.

$$
f_{max,r}(\mathcal{D}) = \frac{w_r}{N_r} \sum_{i=1}^{N_r} (d_i - D_0)^2 * \Theta(d_i - D_0) \quad , \tag{2.19}
$$

$$
f_{min,r}(\mathcal{D}) = \frac{w_r}{N_r} \sum_{i=1}^{N_r} (d_i - D_0)^2 * \Theta(D_0 - d_i) \quad , \tag{2.20}
$$

with d_i, the dose in voxel i and $\Theta(x)$ the Heaviside function is defined as :

$$
\Theta(x) := \begin{cases} 1, & x \geq 0 \\ 0, & x < 0 \end{cases} \quad .
$$

2.10 Robust planning

The use of the Van Herk margin recipe (Section 2.8) works well as long as the margins are chosen adequately with the threshold percentage, the dose distribution is homogeneous, and this distribution is invariant within the threshold percentage of uncertainties [9]. However, due to range uncertainties and the physical nature of

proton beams (*i.e.* the Bragg peak, Figure 2.1), the last assumption is not true for protons [9]. PBS delivery method is even more affected by this issue since the spot weights are defined through optimization (anything that reduces the cost function) and this scheme does not include range uncertainties [9].

As we can see, PTV-based planning raises questions when used with proton therapy [9]. A possible alternative is to plan directly on the CTV and include geometrical uncertainties directly in the optimization scheme [55]. The solution to the minimization problem 2.17 is degenerate; therefore, there are multiple dosimetrically equivalent solutions [55]. Using this degeneracy allows us to reduce the sensitivity to uncertainties when incorporated in the optimization scheme [55]. The latter is called robust planning. Robust planning is based on the implementation of different dose scenarios [45].

Range errors are modelised by [56] :

$$\rho_j = \bar{\rho_j} + \delta_j \sigma_j \ , \tag{2.21}$$

with ρ_j the true range of a beamlet, $\bar{\rho_j}$ the nominal range (*i.e.* the range without uncertainties), σ_j the magnitude of the uncertainties (like described in Section 2.7.1) and δ_j a random variable that determine the strength of the uncertainties. To avoid generating too many scenarios, only the minimum, nominal, and maximum ranges are simulated (Figure B.6).

For setup/range uncertainties, we consider all the displacement of the tumor in a 3D sphere of radius equal to the maximum setup uncertainty [57]. However, to reduce the number of scenarios, we consider that shifts parallel to the beam axis cause an increase/decrease in the air gap which alters the dose minimally. Thus, it is sufficient to only consider displacement in a 2D circle perpendicular to the beam axis. [57]. While this approach allows us to only consider displacement in a circle, the displacement has to be computed in beam eye vue, and therefore the number of beams augments the number of scenarios. The approach taken in Wuyckens *et. al.* [53] is to consider motion in Dicom coordinates in the 3 perpendicular direction positively and negatively. This leads us to a total of 7 scenarios (nominal, +z, -z, +y, -y, +x, -x).

There are multiple optimization schemes related to robust optimization and scenario generation [58], however, we will focus our effort on the one described in the work of Wuyckens *et. al.* [53]. Minimax or worst-case robust optimization is a scheme in which the optimization is done on the worst scenario. It can be done voxel-wise [45], but this leads to non-physical dose distributions [55] and is only of

interest as the lower bound for the worst quality treatment plan [55]. Scenario-wise worst-case robust optimization changes the optimization problem 2.17 into [53] :

$$
\begin{aligned}
&\min_{\mathbf{x}}\{\max_{s\in S}\{f(\mathcal{D},s)\}\} \\
&\qquad\qquad \text{s.t.} \quad \mathcal{D} = \mathcal{B}\mathbf{x} \\
&\qquad\qquad\qquad\quad x \geq 0 \quad \forall x \in \mathbf{x} \\
&\qquad\qquad \text{with} \quad \mathbf{x} \in \mathbb{R}^m, \mathcal{B} \in \mathbb{R}^{N\times m}, \mathcal{D} \in \mathbb{R}^N \\
&\qquad\qquad \text{and} \quad |S| = |S_{setup}| * |S_{random}| \\
&\qquad\qquad \text{with} \quad |S_{setup}| = \#_{step} * 6 + 1, \quad |S_{random}| = 3 \ .
\end{aligned}
\tag{2.22}
$$

The results of robust optimization are reported with DVH bands. These are DVH plots where the area around the curves are the DVHs of the different scenarios (Figure 2.24).

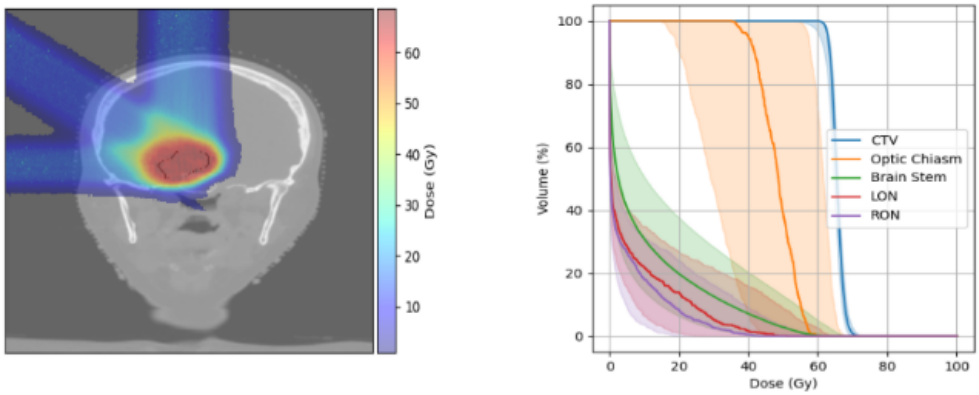

Figure 2.24: DVH bands of a robust optimization with 21 scenarios (7*3), adapted from [53].

Chapter 3

Probabilistic and Radiobiological Optimizations

3.1 The limitation of margins

3.1.1 Clinical to planned target volume extension

Due to the nature of the depth dose distribution of protons versus photons (Figure 2.1), the formalism and the recipe devised for photons cannot be extended to create proton plans [25]. Due to the sharp distal fall-off, proton plans turn out to be even more sensitive to uncertainties [25]. Although some approaches have tried to resolve the PTV described in Section 2.8 by reducing the margin in the direction of the incident beam [59], this approach is only valid for a target covered by a homogeneous dose [60]. PBS being a highly modulated field approach, it is even more affected by range errors (as already mentioned in Section 2.10). Therefore, it seems that a CTV-to-PTV extension is not applicable to planning treatment with protons [25].

An alternative to the use of PTV is planning directly on the CTV with robust planning as described in Section 2.10 [60].

3.1.2 Gross to clinical target volume extension

The current GTV-to-CTV extension like described in Section 2.5.2, follows an all-or-nothing law: the threshold probability of having tumor cells is fixed and the inferred distance from GTV is taken as a margin (Figure 2.17). However, as stated by ICRU:

"The delineation of the CTV is currently based on clinical experience. For quantitative margin definition and future research, it would be advantageous to

introduce a probabilistic definition, e.g., to choose the CTV based on a defined probability of containing clonogenic cells that need to be treated." [15].

Even more, the delineation of the CTV has been found not to be absolute [61]. Although not enough studies have investigated the problem, some have found that the delineated volume could vary between observers by a factor of 1.3 to 2 [61]. The issue could be explained by the fact that the CTV delineation strongly depends on the imaging modality used (as already stated for the GTV in Section 2.5.1).

Moreover, not all types of tumors have the same distribution of clonogenic cells outside the GTV [62]. This difference in the probability of finding clonogenic cells outside the GTV can be translated into the difference in tumor cell density [63]. The effect of this difference in tumor cell density is that the dose needed for an optimal TCP varies with this density [64]. Thus, a lower dose to the region with lower density could achieve the same TCP while sparing more healthy tissues.

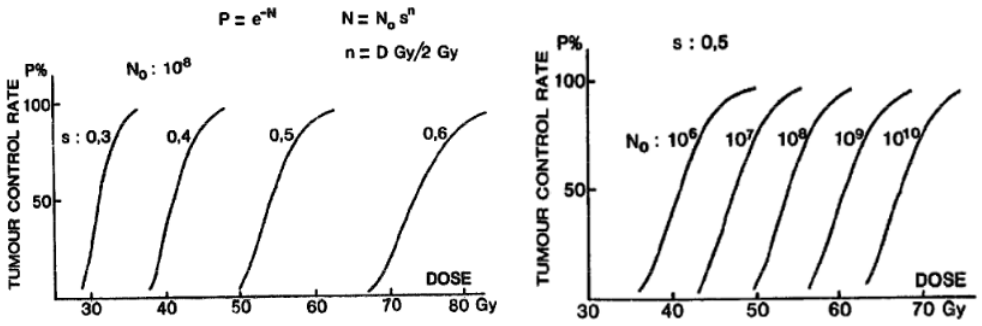

Figure 3.1: TCP curves for different decaying density parameters (above) and different initial density [64].

To motivate the formalism described in Section 3.2, let us introduce the study of Taasti *et. al.* [63]. This study investigates the required margins depending on the distribution of tumor cells in the GTV-to-CTV extension with different dose shapes. The assumption is that, in the GTV, the density of cells is of $10^9 cm^{-3}$ and that in the GTV-to-CTV extension the density follows the following distribution [63]:

$$\rho = \rho_0 \cdot e^{-\lambda \cdot x_{\text{CTV}}} \quad , \tag{3.1}$$

with $\rho_0 = 10^6 cm^{-3}$, x_{CTV} the radial distance from the GTV, λ the density decay parameter, and a cutoff point for CTV $x_{\text{CTV}}^{\max}$.

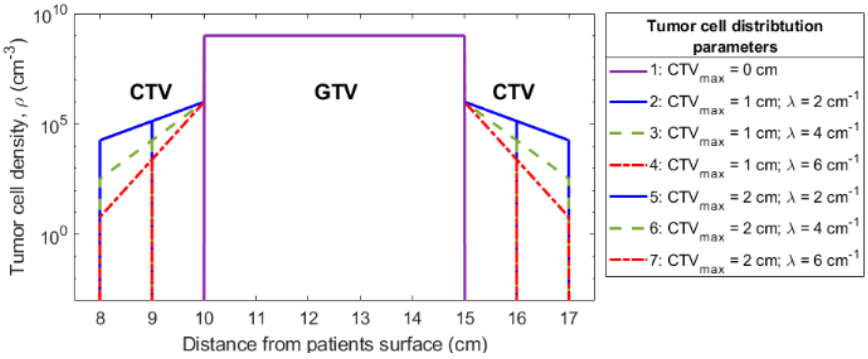

Figure 3.2: The GTV-to-CTV extension with different parameters from supplementary materials of [63].

To account for the number of tumor stem cells surviving in the GTV-to-CTV extension, let us define the clinical control probability (CCP) [63]:

$$\mathrm{CCP}_{\mathrm{CTV}} = \exp(-\sum_{i}^{N_{\mathrm{CTV}}} n_i) \ , \tag{3.2}$$

with n_i the number of tumor stem cells surviving in voxel i. Then, the TCP is rescaled by the CCP [63]:

$$\mathrm{TCP}_{\mathrm{tot}} = \mathrm{TCP}_{\mathrm{GTV}} \cdot (\mathrm{CCP}_{\mathrm{CTV}} \cdot p + (1-p)) \ , \tag{3.3}$$

with $\mathrm{TCP}_{\mathrm{GTV}}$ the TCP in the GTV and p the probability of having tumor cells infiltration outside the GTV.

The purpose of this study is to try to reduce the margins using a smoother distal fall-off of the Bragg peaks. Two opposite beams were used to irradiate a synthetic water equivalent phantom with a tumor of $5 * 5 * 5cm$. Then, imposing a maximum TCP drop of 3%, the margins (m) were reduced with a less steep distal fall-off (Δx). Margins were used to maintain TCP with a range uncertainty of $\pm 3.5\%$ in SPR (with worst-case optimization) [63].
The results show that linear and less steep dose fall-offs are preferred (Figure 3.3) and that a linear dose fall-off can allow reducing margins.

Thus, we can conclude that less aggressive strategies when defining CTV can lead to lower irradiation of surrounding tissue while maintaining desired TCP [63].

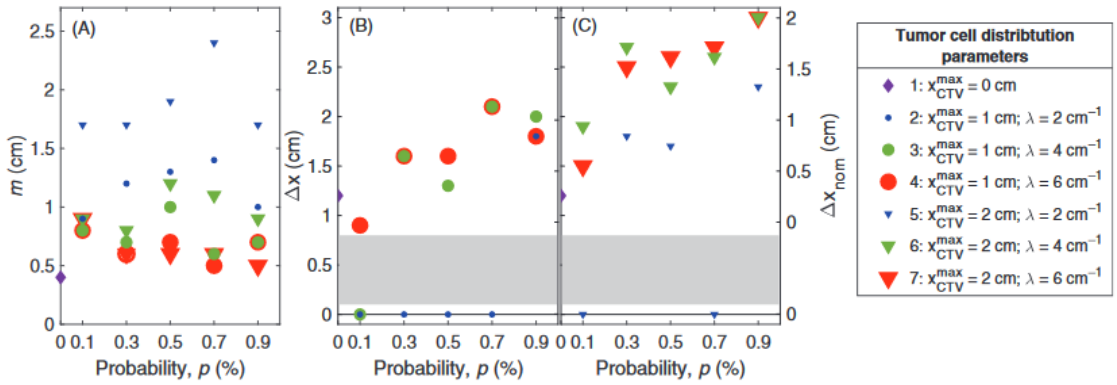

Figure 3.3: Optimization of two opposing proton beams. Margins in function of probability of tumor (A) and the corresponding distal fall-off (B, C) for different density distributions. Gray area corresponds to non-achievable fall-offs. [63]

3.1.3 Need for new definitions of margins

From this prelude on the limitation of margins, we can conclude :

- PTV based planning like defined for photons is inadequate for proton therapy because of the physical nature of interaction of protons and matter (Bragg peak). Robust optimization should be used instead.
- The delineation of CTV is not absolute and varies between observers.
- The definition of CTV is a too aggressive strategy for proton therapy. Even when encompassing range uncertainties, margins can be reduced by using a linear distal fall-off.
- A probabilistic definition of the GTV-to-CTV extension should be preferred and used in optimization.
- TCP is a good indicator of adequate target coverage, but it needs to be scaled to the probabilistic definition of the GTV-to-CTV extension.

3.2 The clinical target distribution

The clinical target distribution (CTD) is a probabilistic definition of the CTV. The CTD formalism has been introduced by Shusharina *et. al.* in their paper *"The clinical target distribution: a probabilistic alternative to the clinical target volume"* [16]. This paper will be the basis for future developments in this master thesis.

As the name suggests, the CTD is an inherently probabilistic concept. It is an alternative to the binary CTV with the probability p_i that the voxel i is tumorous [16, 44, 65]. We will divide our description into three different methods for defining probabilities p_i, two discrete methods, and one continuous.

3.2.1 Discrete probability distributions

We will start by defining the set of shells $\mathcal{H}$ (h_1 the innermost shell being the frontier of the GTV) [16] :

$$\begin{aligned} \mathcal{H} := \{h_1, h_2, ..., h_H\} \\ \text{s.t.} \quad \partial\text{GTV} = \{h_1\} \ . \end{aligned} \tag{3.4}$$

We can also define the set of layer $\mathcal{L}$, the regions in between two shells, each containing N_k voxels [44]:

$$\begin{aligned} \mathcal{L} := \{l_1, l_2, ..., l_{H-1}\} \\ \text{s.t.} \quad \partial l_k = \{h_k; h_{k+1}\} \\ |l_k| = N_k \ . \end{aligned} \tag{3.5}$$

Now let us define the following probabilities :

$$\begin{aligned} P(\text{tumor outside } h_k) = r_k \\ \text{s.t.} \quad r_1 > r_2 > ... > r_H \ , \end{aligned} \tag{3.6}$$

$$\begin{aligned} P(\text{i} \in l_k \text{ tumorous}) = p_{k,i} \\ \text{s.t.} \quad p_{1,i} > p_{2,i} > ... > p_{H-1,i} \\ p_{k,1} = p_{k,2} = ... = p_{k,N_k} \ . \end{aligned} \tag{3.7}$$

The last property of equation 3.7 comes from the fact that we are constructing isoprobabilistic layers of voxels. We can also define the dual of the above probabilities:

$$s_k = 1 - r_k \ , \tag{3.8}$$

$$q_{k,i} = 1 - p_{k,i} \ . \tag{3.9}$$

Independent voxels

If we consider all voxel to be independent, we have [16]:

$$\begin{aligned} s_k &= 1 - r_k \\ &= q_k^{N_k} \\ &\iff q_k = (s_k)^{\frac{1}{N_k}} \ . \end{aligned} \tag{3.10}$$

We now have everything we need to construct those probability shells beginning from the outside [16] :

$$s_{H-k} = q_{H-k}^{N_{H-k}} \cdot s_{H-k+1} \ . \tag{3.11}$$

Hence:

$$q_{H-k} = (\frac{s_{H-k}}{s_{H-k+1}})^{\frac{1}{NH-k}} \ , \tag{3.12}$$

which yields:

$$\begin{aligned} p_{H-k} &= 1 - q_{H-k} \\ &= 1 - (\frac{1 - r_{H-k}}{1 - r_{H-k+1}})^{\frac{1}{NH-k}} \ . \end{aligned} \tag{3.13}$$

Dependent voxels

The dependent voxels approach has been introduced by Buti *et. al.* and is based on the 2 hypotheses [44]:

1. If a voxel is tumorous, all other along the shortest path to the GTV are also tumorous.
2. If a voxel is tumorous, all other voxels from the same layer are also tumorous.

Those assumptions mean that the tumor propagates outwards from the GTV as a front, this is called the contiguous circumferential model [44].

Thus, the probability that there is a tumor outside a shell h_k is equal to the probability that there is no tumor in l_k and outside h_{k+1} [44]:

$$s_k = P(p_{k,i} = 0 \quad \forall i \in l_k \cap s_{k+1} = 0) \ . \tag{3.14}$$

Because both events are dependent in this model:

$$s_k = P(p_{k,i} = 0 \quad \forall i \in l_k) \cdot P(s_{k+1} = 0 \quad | \quad p_{k,i} = 0 \quad \forall i \in l_k) \ . \tag{3.15}$$

Moreover, due to hypothesis (1):

$$P(s_{k+1} = 0 \quad | \quad p_{k,i} = 0 \quad \forall i \in l_k) = 1 \ , \tag{3.16}$$

therefore:

$$s_k = P(p_{k,i} = 0 \quad \forall i \in l_k) \ . \tag{3.17}$$

Also:

$$\begin{aligned} P(p_{k,i} = 0 \quad \forall i \in l_k) &= P(p_{k,i} = 0 \cap p_{k,j} = 0 \quad \forall j \in l_k \backslash i) \\ &= P(p_{k,i} = 0) \cdot P(p_{k,j} = 0 \quad \forall j \in l_k \backslash i \quad | \quad p_{k,i} = 0) \ . \end{aligned} \tag{3.18}$$

And because of the hypothesis (2):

$$P(p_{k,j} = 0 \quad \forall j \in l_k \backslash i \quad | \quad p_{k,i} = 0) = 1 \ , \tag{3.19}$$

therefore :

$$P(p_{k,i} = 0 \quad \forall i \in l_k) = P(p_{k,i} = 0) \ . \tag{3.20}$$

And by definition 3.7:

$$\begin{aligned} P(p_{k,i} = 0) = q_{k,i} \\ \iff P(p_{k,i} = 0 \quad \forall i \in l_k) = q_{k,i} \ . \end{aligned} \tag{3.21}$$

Putting equations 3.17 and 3.21 together gives:

$$s_k = q_{k,i} \ , \tag{3.22}$$

or equivalently :

$$r_k = p_{k,i} \ . \tag{3.23}$$

3.2.2 Continuous probability distribution

Even though those methods allow one to create a probabilistic expansion of the GTV, they still need a physician to delineate the shells of probability. Another method proposed by Buti *et. al.* is to use a continuous definition of the CTD [65]. Let $\rho(x)$ be the Gaussian probability distribution of tumor infiltration (mean and standard deviation taken from the appropriate literature), then we can construct the probability of tumor presence for any voxel [65] :

$$\begin{aligned} p_i(x_i) &= \rho(X \geq x_i) \\ &= \int_{x_i}^{\infty} \rho(x) dx \ , \end{aligned} \tag{3.24}$$

with x_i being the shortest path to the GTV.

3.2.3 Summary of the three methods

To define the probabilities p_i that a voxel is tumorous, we therefore have the 3 following methods.

Discrete method		Continuous method
Tumor islets	Circumferential growth	
$p_{H-k,i} = 1 - (p_{H-k} = \frac{1-r_{H-k}}{1-r_{H-k+1}})^{\frac{1}{NH-k}}$	$p_{k,i} = r_k$	$p_i(x_i) = \int_{x_i}^{\infty} \rho(x)dx$
Shusharina *et. al.* [16]	Buti *et. al.* [44]	Buti *et. al.* [65]
Figure 3.4 (a)	Figure 3.4 (b)	Figure 3.5

Table 3.1: Summary of the different methods to define the voxel probability of being tumorous

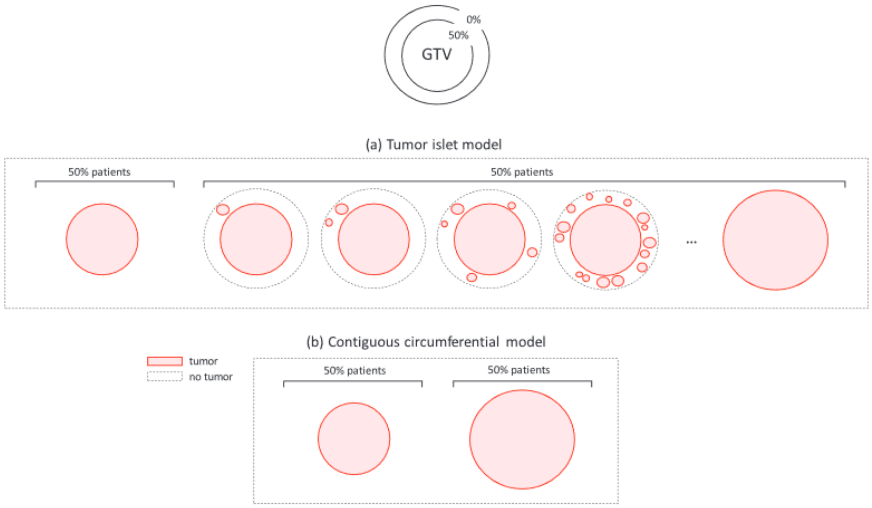

Figure 3.4: Representation of the independent voxel model (a) and circumferential model (b). This is a simplified case with two shells (0% and 50%) [44].

3.3 Probabilistic planning

Now that we have described the CTD formalism, we can proceed with our description of cost functions under the assumption that every voxel has a probability p_i of being tumorous.

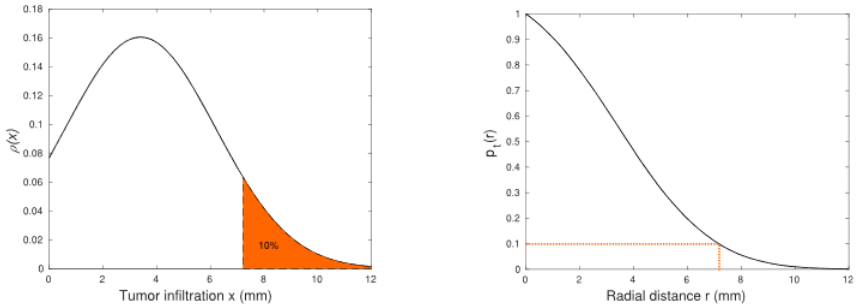

(a) Tumor infiltration uncertainty model. (b) Probability of tumor presence.

Figure 3.5: The probability density function of tumor infiltration (a) with mean 3.4mm and standard deviation 2.8mm. The Gaussian is truncated to avoid negative values. (b) The probability of tumor infiltration according to the above equation. [65]

Generally speaking, probabilistic planning refers to all optimization methods scaled to probabilities. As many methods of probabilistic planning exist, we will focus on two :

- Cost functions adapted to a probabilistic definition of the target volume like described in Section 3.2
- Robust optimization in which each scenario is given a probability of occurring.

The combination of both methods is called *fully probabilistic* optimization [65].

For the cost functions to be adapted to the CTD definition, equations 2.19 and 2.20 become :

$$f_{max-prob,r}(\mathcal{D}) = \frac{w_r}{\sum_{i=1}^{N_r} p_i} \sum_{i=1}^{N_r} p_i (d_i - D_0)^2 * \Theta(d_i - D_0) \ , \tag{3.25}$$

$$f_{min-prob,r}(\mathcal{D}) = \frac{w_r}{\sum_{i=1}^{N_r} p_i} \sum_{i=1}^{N_r} p_i (d_i - D_0)^2 * \Theta(D_0 - d_i) \ . \tag{3.26}$$

As for robust optimization, Buti *et. al.* describes the probability of scenarios the following way [65] :

$$p(s) = p_s(s) \cdot p_r(s) \ , \tag{3.27}$$

with $p(s)$ the probability of the scenario, $p_s(s)$ the probability of setup errors and $p_r(s)$ the probability of range errors. Those probabilities are multiplied because

all the uncertainty sources are considered independent [65]. With a probabilistic framework, the paradigm 2.22 becomes :

$$\begin{aligned} &\min_{\mathbf{x}}\{\mathbb{E}[f(\mathcal{D},s)]\} \\ &\qquad \text{s.t.} \quad \mathcal{D} = \mathcal{B}\mathbf{x} \\ &\qquad\qquad x \geq 0 \quad \forall x \in \mathbf{x} \\ &\qquad\qquad \mathbb{E}[f(\mathcal{D},s)] = \sum_{s\in S} p(s) f(\mathcal{D},s) \\ &\qquad \text{with} \quad \mathbf{x} \in \mathbb{R}^m, \mathcal{B} \in \mathbb{R}^{N\times m}, \mathcal{D} \in \mathbb{R}^N, p(s) \in \mathbb{R} \ . \end{aligned} \tag{3.28}$$

This paradigm is called expected value optimization. However, to provide control over the degree of robustness, one could change paradigm 3.28 into [65] :

$$\begin{aligned} &\min_{\mathbf{x}}\{(1-\lambda)\mathbb{E}[f(\mathcal{D},s)] + \lambda\sqrt{\mathbb{V}[f(\mathcal{D},s)]}\} \\ &\qquad \text{s.t.} \quad \mathcal{D} = \mathcal{B}\mathbf{x} \\ &\qquad\qquad x \geq 0 \quad \forall x \in \mathbf{x} \\ &\qquad\qquad \mathbb{E}[f(\mathcal{D},s)] = \sum_{s\in S} p(s) f(\mathcal{D},s) \\ &\qquad\qquad \mathbb{V}[f(\mathcal{D},s)] = \sum_{s\in S} (p(s) f(\mathcal{D},s) - \mathbb{E}[f(\mathcal{D},s)]^2) \\ &\qquad \text{with} \quad \mathbf{x} \in \mathbb{R}^m, \mathcal{B} \in \mathbb{R}^{N\times m}, \mathcal{D} \in \mathbb{R}^N, p(s) \in \mathbb{R}, \lambda \in \mathbb{R} \ . \end{aligned} \tag{3.29}$$

This other paradigm is called expected value - standard deviation optimization. The parameter λ is user defined and allows one to trade off between the expected conformity of the treatment and the risk [65].

Although the methods described here allow us to scale the dose optimization to probabilities, one still needs an efficient way to assess for plan quality. Because in an optimal plan, the dose is scaled to the probabilities (equations 3.25 and 3.26), therefore the DVHs (like described in Section 2.6) can no longer be used as it. Indeed, target volumes with a lower probability will receive a lower dose, penalizing the DVH curve. A fix proposed by Buti *et. al.* is to translate DVH into dose expected volume histogram (DEVH) [44]. Then equation 2.13 becomes :

$$\mathbb{E}[h_k] = \sum_{i=1}^{N} p_i \delta_{k,\kappa(d_i)} \ . \tag{3.30}$$

The equation 2.14 also has to be modified for the expected bins value but also to account that the "accessible volume" is no longer N :

$$\mathrm{DEVH}_k = \frac{100\%}{\sum_{i=1}^{N} p_i} \sum_{j=k}^{K} \mathbb{E}[h_k] \ . \tag{3.31}$$

3.4 Radiobiological optimization

Until now, all the optimization methods described relied on dose prescriptions and penalized for divergence of these prescriptions (equations 2.19 and 2.20). Methods based on dose prescriptions are the clinical routine [15]. However, ultimately, tumor regression and radiation toxicity are determined by biological mechanism [66], which could raise questions about the legitimacy of dose constraint optimizations.

Radiobiological-based optimizations allow encompassing personalized inhomogene tumor risk and toxicity due to volume dependence [67]. It also allows for exploring the trade-offs between tumor cure and toxicity to normal tissues [67].

3.4.1 Radiobiological models

There exist many models to express the sigmoidal curves (Figure 2.8) of TCP and NTCP [13] but we will stick with the definitions that depend on the linear quadratic surviving fraction described in equation 2.3.

Control of the tumor can be seen as the probability of killing all clonogenic cells within the target volume. Munro and Gilbert based their model on the assumption that the cell killing process is stochastic and follows a Poisson distribution [11]:

$$TCP = e^{-\lambda} \ , \tag{3.32}$$

with λ the average number of surviving cells [67], which is precisely the equation 2.3. Hence, the TCP can be expressed as :

$$TCP(D) = e^{-N_0 e^{-\alpha D - \beta D^2/n}} \ , \tag{3.33}$$

with N_0 the initial number of clonogenic cells. Now we can compartmentalize this model for a volume composed of N voxels with relative volume v_i, and because the TCP is a probability, it means that we can multiply each independent TCP of each voxel [13]:

$$\begin{aligned} TCP(\mathcal{D}) &= \prod_{i=1}^{N} TCP_i \\ &= e^{-N_0 \sum_{i=1}^{N} v_i e^{-\alpha d_i - \beta d_i^2/n}} \quad . \end{aligned} \tag{3.34}$$

There also exist many NTCP models since the definition of normal tissue complication is vague. As some models use binary endpoints or population statistics [67], we will stick with a model based on equation 2.3 to stay consistent with the above-mentioned TCP model.

NTCP is based on the ability of an organ to remain functional after irradiation. Therefore, we have to introduce the concept of organ seriality. A serial organ (*e. g.* the spinal cord) will stop functioning if one if his "chain link" is destroyed, while a parallel organ (*e. g.* the liver) will remain functional. This concept of seriality allows us to define the "relative seriality" for an organ viewed as an m by n matrix (Figure B.8) as [68] :

$$s = \frac{m}{mn} = \frac{1}{n} \quad . \tag{3.35}$$

The probability of radiation injury for parallel and serial organs have been derived by Källman *et. al.* [12] as :

$$P_{\text{serial}}(D) = 1 - \prod_{i=1}^{m} (1 - P_i) \quad , \tag{3.36}$$

$$P_{\text{parallel}}(D) = \prod_{i=1}^{n} P_i \quad . \tag{3.37}$$

Combining equations 3.36 and 3.37 with the linear quadratic formula 2.3 and the assumption that cell death follows a Poisson distribution gives the NTCP voxel-wise model [12, 13] :

$$NTCP(\mathcal{D}) = [1 - \prod_{i=1}^{N} (1 - [e^{-N_0 e^{-\alpha d_i - \beta d_i^2/n}}]^s)^{v_i}]^{\frac{1}{s}} \quad . \tag{3.38}$$

Now, for multiple OARs with different biological parameters, the total NTCP can be computed as [13] :

$$NTCP(\mathcal{D}) = 1 - \prod_{j=1}^{S} [1 - NTCP_j(\mathcal{D})]^{\xi_j} \quad , \tag{3.39}$$

for S OARs with their relative severity of injuries ξ_j such that $\sum_{j=1}^{S} \xi_j = 1$.

UTCP is the probability of having a complication-free tumor control or, in more general terms, a complication-free treatment. For the convenience of the following demonstration, let us switch that reflects the probabilistic nature of TCP, NTCP and UTCP more :

$$\begin{aligned} P(TC) &:= TCP \\ P(NTC) &:= NTCP \\ P(UTC) &:= UTCP \ . \end{aligned} \tag{3.40}$$

Ågren *et. al.* defined the probability of complication-free treatment as [69] :

$$P(UTC) = P(TC) - P(TC \cap NTC) \ , \tag{3.41}$$

which can be extended as :

$$\begin{aligned} P(UTC) &= P(TC) - P(TC) \cdot P(NTC \mid TC) \\ &= P(TC)[1 - P(NTC \mid TC)] \\ &= P(TC)[1 - \frac{P(NTC)P(TC \mid NTC)}{P(TC)}] \ . \end{aligned} \tag{3.42}$$

We now have two limiting cases; either the probability of radiation-induced injuries to normal tissue is totally decorallated to tumor control ($TC \perp NTC$) either, the two are totally correlated ($TC \not\perp NTC$). Those give [69] :

$$\begin{aligned} TC \perp NTC \iff & P(TC \mid NTC) = P(TC) \\ \Rightarrow & P(UTC)_1 := P(TC)[1 - P(NTC)] \ , \end{aligned} \tag{3.43}$$

$$\begin{aligned} TC \not\perp NTC \iff & P(TC \mid NTC) = 1 \\ \Rightarrow & P(UTC)_0 := P(TC) - P(NTC) \ . \end{aligned} \tag{3.44}$$

Because one cannot assume the dependence of TC and NTC, the proposition of Ågren *et. al.* is to define a parameter δ that accounts for the degree of dependence of TC and $NTCP$ in a mixed population [69] :

$$P(UTC) = (1 - \delta)P(UTC)_0 + \delta P(UTC)_1 \ , \tag{3.45}$$

or going back to definitions 3.40 :

$$UTCP = (1 - \delta)[TCP - NTCP] + \delta[TCP[1 - NTCP]] \ . \tag{3.46}$$

The effect of δ on UTCP will be to lower the curve if TCP and NTCP are completely correlated (Figure B.9).

3.4.2 Equivalence of tumor control probability and dose prescription

As can be seen, both TCP and NTCP are strongly dependent on the α and β parameters. Although voxel-based and not population-based, Shinkel *et al.* have shown that if not used to fit α and β, equations 3.34 and 3.38 are valid approximations of population-based models [70]. Yet, to discuss our later results, it might be tempting to derive the dose needed for a threshold TCP depending on the volume and the $\frac{\alpha}{\beta}$ ratio. So, let:

$$D_{50} \text{ s. t. } TCP(D_{50}) = 50\% \ , \tag{3.47}$$

with the 50% threshold chosen because of its use in other TCP models [13]. Then from equation 3.34, if we assume the same dose for each voxel in the target and that voxels are isotropic, we get :

$$\begin{aligned} 50\% &= e^{-N_0 \sum_{i=1}^{N} v_i e^{-\alpha D_{50} - \beta D_{50}^2/n}} \\ &= e^{-N_0 e^{-\alpha D_{50} - \beta D_{50}^2/n}} \end{aligned} \tag{3.48}$$

$$\begin{aligned} ln(\frac{-ln(50\%)}{N_0}) = & -\alpha D_{50} - \frac{\beta}{n} D_{50}^2 \\ & \Big\downarrow \zeta_{50} := ln(\frac{-ln(50\%)}{N_0}) \\ 0 = & \frac{\beta}{n} D_{50}^2 + \alpha D_{50} + \zeta_{50} \ . \end{aligned} \tag{3.49}$$

This leads us to the two forms :

$$\frac{\alpha}{\beta} = -\frac{\alpha D_{50}^2}{n\alpha D_{50} + n\zeta_{50}} \ , \tag{3.50}$$

and :

$$D_{50} = -\frac{n}{2}\frac{\alpha}{\beta} + \frac{n}{2\beta}\sqrt{\alpha^2 - \frac{4\beta\zeta_{50}}{n}} \ , \tag{3.51}$$

taking only the positive part of the root to avoid negative doses.

As we can see, the dose needed for a TCP of 50% is lower with less fraction (Figure 3.6). Although it may be tempting to reduce the number of fractions, we have to bear in mind that fractionated treatments allow for a better NTCP.

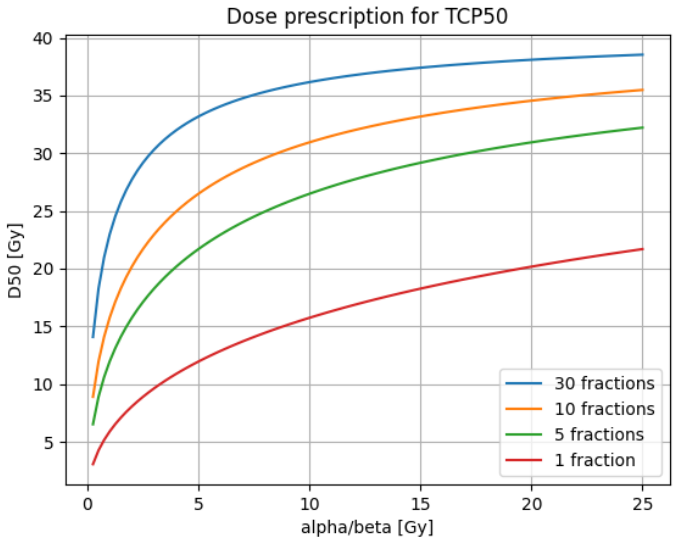

Figure 3.6: D_{50} depending on the ratio $\frac{\alpha}{\beta}$ (for $\alpha = 0.35[Gy]^{-1}$). The volume is $100mm^3$ and $N_0 = 10^7 cm^{-3} \cdot 100mm^3 = 10^6$.

3.4.3 State of the art : biological optimization

As mentioned above, dosimetric considerations alone are not sufficient to find the optimal plan, simple examples can easily demonstrate that dose constraint optimization can create results that contradict TCP [66]. Let us imagine that a plan irradiates all voxels of the tumor but one; dose-based cost function would have a reasonable low total if the dose is close to the prescription. But because tumors can be seen as parallel structures [67], the TCP would be null.

Let us create another simple example to prove the need for biological optimization. Let a beam go through two voxels one being the tumor and the other an OAR. Then if we create a simple model with $TCP = \frac{1}{1+\frac{D_{50}}{10D}}$ (a simpler model of the TCP, close to the ones in Bentzen *et. al.* [67] but sufficient for our example). We also define the maximum dose to the OAR as $20Gy$, the minimum dose to the target $70Gy$, the $D_{50} = 50Gy$ and a TCP_{min} of 95%. The cost functions penalize for the square of the deviation of the desired dose or TCP. We see in Figure 3.7, that the results with dose-only constraints do not allow for a sufficient TCP.

Thus, the addition of biological criteria in optimization allows one to explore a larger solution space than dose-constrain-based optimization and find solutions that violate the dose constraint but are biologically better [66].

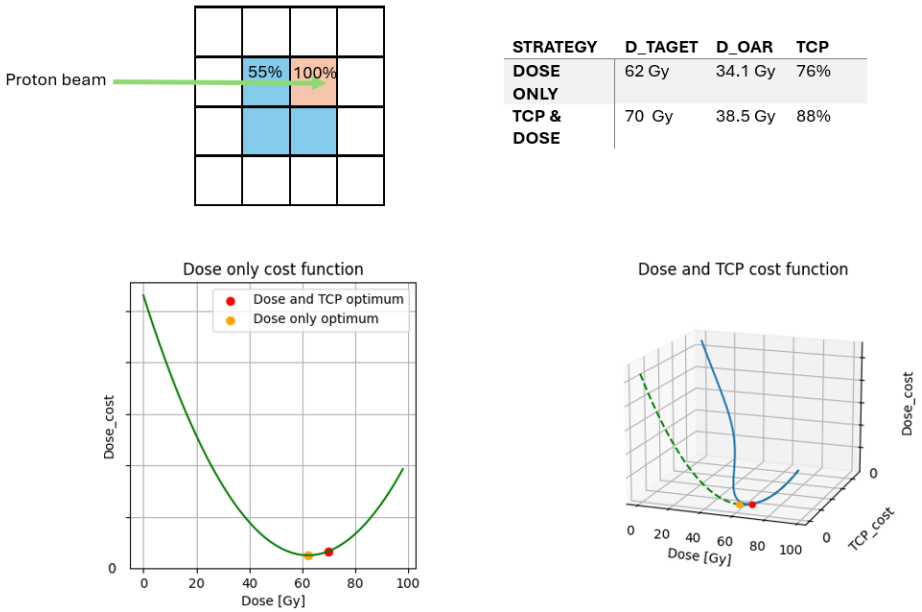

Figure 3.7: Simple toy example of dose-based and biological-based optimization. The target is in orange, and the OAR is in blue. The Bragg peak is set so that the target receives 100% of the dose and the OAR 55%.

The problem of biological optimization is that TCP and NTCP, as presented in Section 3.4.1, are non-convex [13]. Although they can be made convex like proposed by Hoffman *et. al.* [13] there is an alternative pathway for TCP optimization. Since it has long been proven that a uniform dose to the target gives the highest TCP [71], one might be tempted to use an even more thorough concept: equivalent uniform dose (EUD). The EUD is the homogene dose that will give the same radiobiological effect as the dose distribution $\mathcal{D}$ [72, 66]. The definition of the EUD depends on the radiobiological model chosen. An EUD defined by the SF (equation 2.3) has been derived by McGary *et. al.* [73, 13] :

$$EUD(\mathcal{D}) = -\frac{1}{2}\frac{\alpha}{\beta}n[1 - \sqrt{1 - \frac{4\beta}{\alpha^2 n}ln(\overline{SF(\mathcal{D})})}] \ , \tag{3.52}$$

with :

$$\overline{SF(\mathcal{D})} = \sum_{i=1}^{N} v_i e^{-\alpha d_i - \beta d_i^2/n} \ . \tag{3.53}$$

We can return to equation 3.51 if $\zeta_{50} = \overline{SF(\mathcal{D})}$. The interpretation is that ζ_f for any prescription f is the logarithm of the desired fractions of cells to kill.

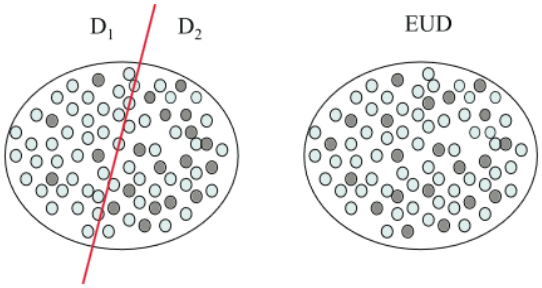

Figure 3.8: Equivalent uniform dose based on the surviving fraction [66]. The EUD is the dose that kills the same number of cells (dark dots) than D_1 and D_2.

In terms of NTCP, the problem is that a simple NTCP optimization assumes that all complications are of the same severity, which is not the case [66], and that the injury correlates with radiation where the patient's history needs to be taken into account [66].

One of the proposed solutions to the problems of TCP and NTCP optimization described above is the use of sub-scores based on different criteria (TCP, EUD, NTCP, DMAX, DMIN, ...) such that the final score is the multiplication of each sub-score [66]. But the central problem of this approach is the assignment of weighting factors [66]. Indeed, comparing different objectives that are based on biological models and physical models leads to arbitrary decisions when choosing weights [66].

Finally, regarding UTCP optimization, Kim *et. al.* have proven through the use of a subvolume based TCP model and a voxel-based NTCP model that the impact of the δ parameter in equation 3.46 has little impact in optimization, and therefore setting $\delta = 1$ is enough [14]. This is convenient because $UTCP_0$, contrary to $UTCP_1$, cannot be convexified [13].

3.4.4 Probabilistic radiobiological models

To account for the probabilistic definition of our target as described in Section 3.2, we have to slightly modify the definition of our TCP model 3.34. It would seem logical, but to have a TCP that is rescaled to the probability that a voxel will be tumorous, similar to the equation 3.3. We also have to account for the fact that if a voxel is not tumorous, his TCP must equal 1 [16]. The model proposed by Shusharina *et. al.* [16] is:

$$PTCP_i = (1 - p_i) + p_i TCP_i \ , \tag{3.54}$$

$$PTCP(\mathcal{D}) = \prod_{i=1}^{N}((1-p_i) + p_i e^{-N_0 v_i e^{-\alpha d_i - \beta d_i^2/n}}) \ , \tag{3.55}$$

where we have chosen to introduce the notation $PTCP$ for later convenience.

3.4.5 State of the art : probabilistic radiobiological optimization

When considering probabilistic radiobiological planning, it is important to be aware that the methods of defining the CTD as described in Section 3.2 will not have the same effect on the TCP. Indeed, with the independent voxels model, underdosing a few voxels of the CTD will result in a small TCP loss due to the small probabilities of those voxels [44]. This will allow for better OAR sparing. For the dependent voxels model, the probabilities are high, thus underdosing few voxels will have more effect on the TCP and thereby reduces the OAR sparing [44]. Although the latter could be improved by using the dose fall-off to dose the outer layers of the CTD [44], which is precisely what we seek.

Direct radiobiological optimizations oppose several problems. First of all, there exists no probabilistic definition of the EUD defined in equation 3.52. It exists some EUD developments that account for population inhomogeneity [72], but none of them includes the probability that a cell is tumorous. This is because EUD refers to the number of cells killed, regardless of whether they are tumorous or not. Second, the PTCP described in equation 3.55 is not convex and cannot be convexified with the same TCP reformulation [13, 17]. Finally, the PTCP mentioned above is true for independent voxels (Section 3.2), but for dependent voxels, the dependency must be carried out in the PTCP model. Let us compute the PTCP for one of the outer layers l_k. Recalling the hypothesis of the dependent voxels, if l_k is tumorous, all other voxels along its path to the GTV are also tumorous. Therefore, the probability that the tumor does not extend further is $p_k - p_{k+1}$. Thus, the PTCP is [17]:

$$PTCP_k = (p_k - p_{k+1}) \prod_{j=1}^{k} TCP_j \ , \tag{3.56}$$

hence, the total PTCP :

$$PTCP_{tot} = \sum_{i=0}^{N_k}[(p_i - p_{i+1}) \prod_{j=1}^{i} TCP_j] \ , \tag{3.57}$$

with the boundaries :

$$\begin{aligned} l_0 &= \text{GTV} \\ p_0 &= 1 \\ p_{N_k+1} &= 0 \ . \end{aligned} \tag{3.58}$$

Note that TCP_j is the TCP of a layer, which is the multiplication of all TCP_i of voxels of this layer (equation 3.34).

To the best of our knowledge, the only article that has studied the optimization of PTCP is by Bortfeld *et al.* [17].It is important to mention that this study has been carried out for conventional radiotherapy and not proton therapy. To try to incorporate some dose constraint into the PTCP optimization, the authors have used the Lagrange multiplier method. The idea is to transform :

$$\begin{aligned} &\max_{\mathcal{D}}[\sum_i^N ln(PTCP(d_i))] \\ &\qquad \text{s. t.} \quad \sum_i^N d_i = D_0 \ , \end{aligned} \tag{3.59}$$

into :

$$\mathcal{L}(\mathcal{D}) = \sum_i^N ln(PTCP(d_i)) + \lambda(\sum_i^N d_i - D_0) \ , \tag{3.60}$$

$$\frac{\partial \mathcal{L}}{\partial d_i} = 0 \quad \frac{\partial \mathcal{L}}{\partial \lambda} = 0 \ . \tag{3.61}$$

Imposing the conditions 3.61 on the derivatives allows us to find the optimal solution [74]. One might notice that the derivation of the PTCP with respect to the dose is tedious for the dependent voxels model. As an approximation, it is possible to use the Taylor first-order approximation $e^x = 1 - x$ because of the high dose. This leads to the approximation of PTCP [17] :

$$PTCP(\mathcal{D}) \approx 1 - \sum_i^N p_i TCP_i(d_i) \ . \tag{3.62}$$

With this optimization setup, the authors have tried to compare those optimization results with a heuristic strategy of sacrificing subvolumes where PTCP could not improve anymore. They used a cylindrical phantom with 4 OARs (Figure 3.9), restricted the dose to the GTV to 64 Gy and varied the limit on the total mean dose [17]. Their results showed that at higher doses there is no significant difference between the independent and dependent voxel models (Figure 3.9).

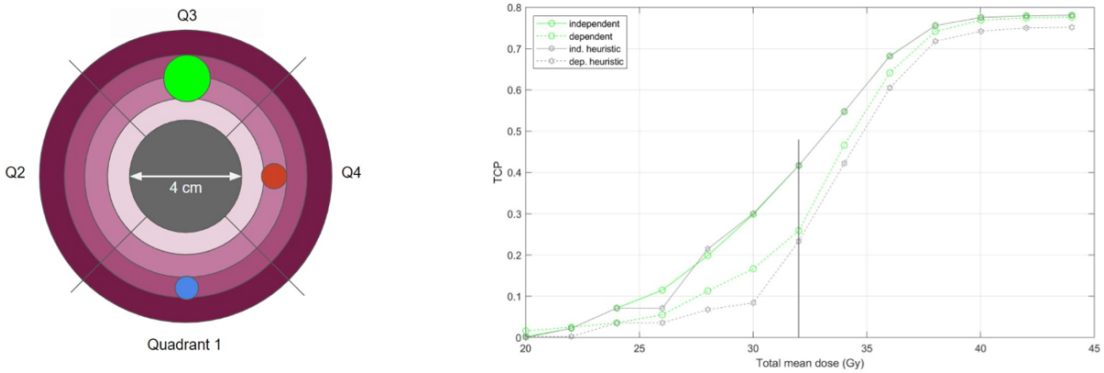

Figure 3.9: Left, synthetic phantom with the GTV (gray), CTD layers (purple) and the 3 OARs (circles). Right, the TCP in function of the mean dose for independent and dependent voxel models for the two strategies described above.

As mentioned above, this study is the only one that has investigated direct PTCP optimization, but the question of the feasibility of this method for proton therapy remains open. Even more, the impact of this optimization on OAR has not yet been studied.
Prospects of a NTCP and PTCP combination for a direct UTCP optimization with protons have yet to be investigated.

Chapter 4

Materials and Methods

4.1 Materials

4.1.1 OpenTPS

OpenTPS [53] is an open-source software platform designed for proton therapy treatment planning. It offers a comprehensive suite of tools to simulate, optimize, and evaluate radiation treatment plans. OpenTPS v1.1.0 was used in this thesis to implement and evaluate a new probabilistic optimizer and introduce new radiobiological objectives (TCP / NTCP) for optimization.

4.1.2 Phantom and head and neck CT

For the purpose of our work, we first used a synthetic phantom to develop our optimizer as it was faster to compute and optimize on small images. When our results with the OAR were convincing, we switched to a real head and neck CT.

The synthetic phantom (Figure 4.1) is a square box of size $128mm \times 128mm \times 128mm$ with a squared 'body' of $105mm \times 105mm \times 105mm$. In the center of this box, we placed a spherical tumor, representing the GTV, with a radius of 8mm. In addition, we placed a rectangular parallelepipedal OAR near the tumor.

For the CT scan (Figure 4.2), we used data from a head and neck cancer patient, where the different ROIs had already been delineated. This CT has been provided by the Molecular Imaging and Radiation Oncology (MIRO) laboratory of the *Institut de recherche Experimentale et Clinic* (IREC) of UCLouvain. This scan has been anonymized and comes from the dataset used in Huet *et. al.* [75].

We considered the entire body as an OAR but excluded the calculation of the NTCP within a 10 mm margin from the edge of the GTV. This margin was set because it is not meaningful to calculate NTCP in areas where tumor treatment is intended. Although a probabilistic NTCP approach could be a suitable alternative, it falls outside the scope of this thesis. The rest of the selected OARs are listed in the table C.1.

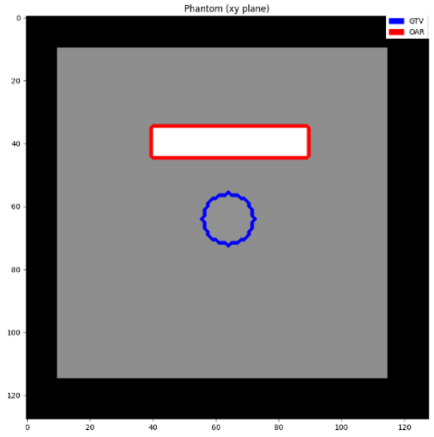

Figure 4.1: Phantom with GTV (blue) and OAR (red) contours

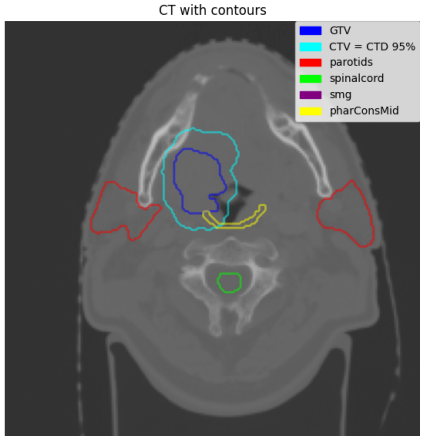

Figure 4.2: Contours in the head and neck CT.

4.1.3 Clinical Target Distribution

The independent voxel model is generally associated with probabilities ranging from 10^{-5} to 10^{-6} [44], these small probabilities oppose the problem of vanishing gradient for the optimization (derivations in the next section); thus we opt for the dependent voxel model to define the layers of the CTD. To compute the probabilities associated with each layer, we used an approach similar to the continuous probability distribution (Section 3.2).

Under the assumption of a Gaussian (pdf) distribution for tumor infiltration around the GTV, with a mean displacement of 2 mm and a standard deviation of 1.8 mm, the corresponding probability of tumor presence is the cumulative density function obtained from the Gaussian distribution mentioned above (Figure 4.3). We used a 1D Gaussian truncated distribution to have a smoother decay in probability. The mean and standard deviation were selected to have a probability of tumor presence of 5% at 5 mm to follow clinical practice [76].

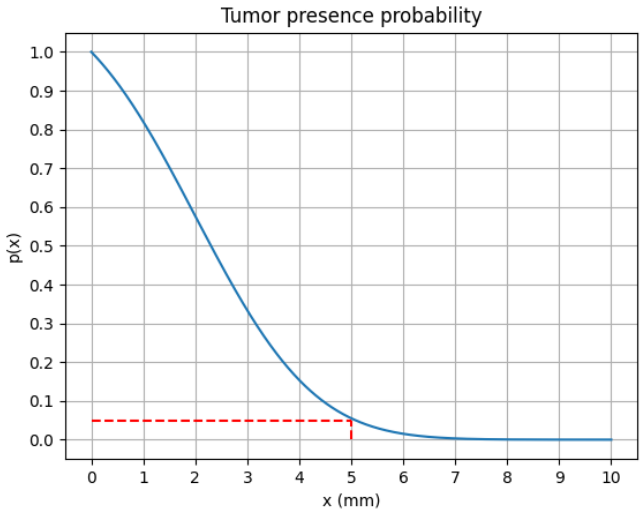

Figure 4.3: Probability of a voxel being cancerous as a function of its distance from the GTV edge. The standard GTV-CTV margin (5% chance of tumor presence) is indicated at 5 mm.

Here, we performed dilation in increments of 1 mm. For each millimeter of expansion, the new voxels added to the mask are given a probability $p(x)$ of tumor presence, where x is the number of millimeters of dilation from the edge of the GTV (Figure 4.4).

Dilation is a technique used to expand the boundaries of a tumor mask. A tumor mask is a binary image in which the tumor is marked with a value of 1, and the surrounding tissue is marked with a value of 0. By dilating the tumor mask, we incrementally add layers of voxels in 3D around the tumor's edge.

OpenTPS does not allow one to create an objective on a probability map, so we had to use a binary mask for the computation. We then define the limit as the volume in which the probability of tumor presence $>= 5\%$ is present (to follow the conventions of the expansion of the CTV described in Section 2.5.2) and there is no correction for the presence of OAR in this volume.

4.1.4 Independent voxel tumor control with dependent voxel model

As mentioned earlier, equation 3.57 is not easily derivable and its "ln form" to try to resemble the convex TCP formulation would lead to non-practical derivatives.

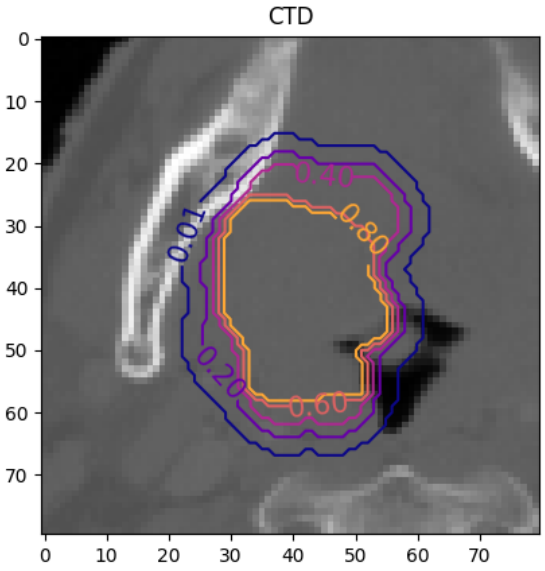

Figure 4.4: CTD expansion of the GTV for the considered CT.

The approximation proposed in equation 3.62 would also not allow simplifications in the derivative in its "*ln* form." The importance of using the logarithm of the PTCP is to a quantity comparable to NTCP and, therefore, avoid as much as possible arbitrary weights.

One way around those problems is to use the PTCP model 3.55 derived for independent voxels. Even though we lose the sense of the PTCP metric by violating the non-tunneling hypothesis, optimization through the use of the PTCP model for independent voxel is less punitive for outer layers. The optimization scheme fosters local (layer-wise) tumor control, which resembles the heuristic approach of sacrificing volume described by Bortfeld *et. al.* [17].

One could also notice that equation 3.55 is close to equation 3.3 if the density decay parameter λ is set to 0 and the surviving fraction 2.3 is taken into account. The authors of the study [63] have shown that layers outside the GTV could be treated by a less steep dose fall-off. Thus, extending to several layers instead of one for CCP using the PTCP model 3.55 would allow reducing the dose to layers with lower probabilities, while maintaining adequate TCP but, above all, improving the OAR sparing problem of the dependent voxel model [18].

4.1.5 Uncomplicated Tumor Control Probability optimization

In order to optimize UTCP while encompassing the definition of the PTCP, we defined PUTCP as :

$$PUTCP := PTCP \cdot (1 - NTCP) \ , \tag{4.1}$$

where one can notice that we directly started from the definition of $UTCP_0$ because the parameter δ does not affect the optimization as stated earlier. Recalling equation 3.55, we define a weight w_t to be able to balance PTCP and NTCPs :

$$PTCP(\mathcal{D}) = (\prod_{i=1}^{N_t}((1 - p_i) + p_i e^{-N_0 v_i e^{-\alpha d_i - \beta d_i^2/n}}))^{w_t} \ , \tag{4.2}$$

with N_t the number of voxels in the target (GTV and CTD). The weight has been set as an exponent for later convenience in the "ln-form." Now recalling equation 3.39, NTCP is defined as :

$$NTCP(\mathcal{D}) = 1 - \prod_{j=1}^{S}[1 - NTCP_j(\mathcal{D})]^{\xi'_j} \ , \tag{4.3}$$

where we defined ξ'_j as :

$$\xi'_j := \xi_j w_j \ , \tag{4.4}$$

with ξ_j the partial volume of OAR j and w_j the weight of OAR j. We used this definition of ξ_j to ensure that all OARs no matter their volume are treated equivalently. The addition of weights w_j is to "direct" the optimization scheme towards the desired solution.
Now, to use a more easy form of the NTCP, we will make two assumptions: (1) the injuries of the cells in a voxel are parallel, (2) the injuries between the voxels are serial (s=1). This allows us to rewrite the equation 3.39:

$$\begin{aligned} NTCP(\mathcal{D}) &= 1 - \prod_{j=1}^{S}[1 - NTCP_j(\mathcal{D})]^{\xi'_j} \\ &= 1 - \prod_{j=1}^{S}[\prod_{i=1}^{N_j} 1 - [e^{-N_0 v_i e^{-\alpha d_i - \beta d_i^2/n}}]]^{\xi_j w_j} \ . \end{aligned} \tag{4.5}$$

4.2 Optimization scheme

4.2.1 Convex reformulation

The main challenge with the $PTCP/NTCP$ functions is their non-convex nature [13, 17]. This non-convexity can make optimization difficult because standard gradient descent methods might get stuck in local minimums rather than finding the global minimum.

However, research by Hoffman *et. al.* [13] has shown that $-ln(NTCP)$ and $-ln(TCP)$ are convex. Unfortunately, $-ln(PTCP)$ is not convex. Despite this, optimization does not pose a significant issue because the shape of the $-ln(PTCP)$ function is such that it guides the optimization process toward a region close to the global minimum. This characteristic allows gradient descent optimization to converge to a solution that is near optimal, even if it is not the absolute global minimum.

Thus, the non-convexity of $PTCP$ does not prevent effective optimization. By carefully structuring our optimization problem and leveraging the properties of the function, we can still achieve a highly effective solution to balance PTCP and NTCP.

$$-ln(PUTCP(\mathcal{D})) = -ln(PTCP(\mathcal{D})) - ln(1 - NTCP(\mathcal{D})) \ , \tag{4.6}$$

with

$$\begin{aligned} -ln(PTCP(\mathcal{D})) &= -ln((\prod_{i=1}^{N_t}((1-p_i) + p_i e^{-N_0 v_i e^{-\alpha d_i - \beta d_i^2/n}}))^{w_t}) \\ &= -w_t \sum_{i=1}^{N_t} ln((1-p_i) + p_i e^{-N_0 v_i e^{-\alpha d_i - \beta d_i^2/n}})) \ , \end{aligned} \tag{4.7}$$

and

$$\begin{aligned} -ln(1 - NTCP(\mathcal{D})) &= -ln(1 - (1 - \prod_{j=1}^{S}[\prod_{i=1}^{N_j} 1 - [e^{-N_0 v_i e^{-\alpha d_i - \beta d_i^2/n}}]]^{\xi_j w_j})) \\ &= -\sum_{j=1}^{S} \xi_j w_j \sum_{i=1}^{N_j} ln(1 - [e^{-N_0 v_i e^{-\alpha d_i - \beta d_i^2/n}}]) \ . \end{aligned} \tag{4.8}$$

Because voxels are isotropic, we can introduce the parameter $\eta = N_0 \cdot v_i$ the number of cells per voxel. This leads us to the following:

$$-ln(PTCP(\mathcal{D})) = -w_t \sum_{i=1}^{N_t} ln((1-p_i) + p_i e^{-\eta e^{-\alpha d_i - \beta d_i^2/n}})) \ , \tag{4.9}$$

$$-ln(1 - NTCP(\mathcal{D})) = -\sum_{j=1}^{S} \xi_j w_j \sum_{i=1}^{N_j} ln(1 - e^{-\eta e^{-\alpha d_i - \beta d_i^2/n}}) \ . \tag{4.10}$$

We can then conveniently use equation 3.34 to simplify into :

$$-ln(PTCP(\mathcal{D})) = -w_t \sum_{i=1}^{N_t} ln((1 - p_i) + p_i TCP_i(d_i)) \ , \tag{4.11}$$

$$-ln(1 - NTCP(\mathcal{D})) = -\sum_{j=1}^{S} \xi_j w_j \sum_{i=1}^{N_j} ln(1 - TCP_i(d_i)) \ , \tag{4.12}$$

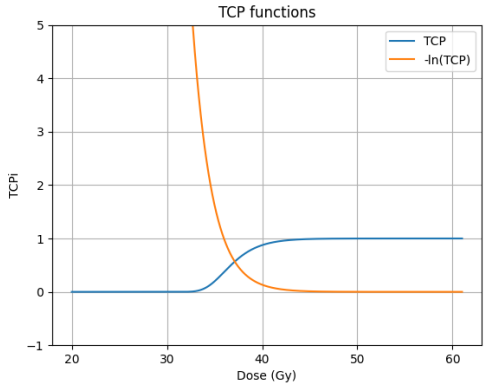

Figure 4.5: TCP and -ln(TCP) functions

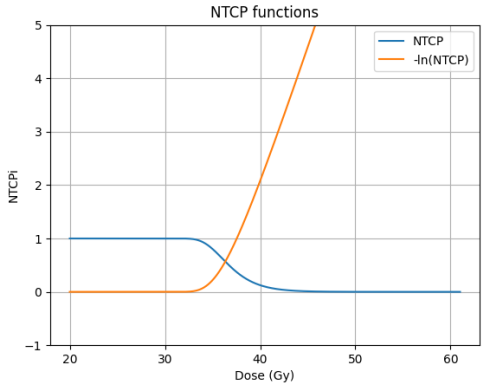

Figure 4.6: NTCP and -ln(NTCP) functions

4.2.2 Gradient descent

To optimize the function 4.6, we used a gradient descent method. We relied on the provided L-BFGS method in the *scipy* library based on the Broyden–Fletcher–Goldfarb–Shanno algorithm [77].

We computed the derivatives of equations 4.11 and 4.12. To ensure positive beamlets weight (as a negative weight would have no physical sense), we introduced $\mathbf{u} \in \mathbb{R}^m$:

$$\mathbf{u} \text{ s. t. } \forall x_i \in \mathbf{x}, u_i^2 = x_i \ . \tag{4.13}$$

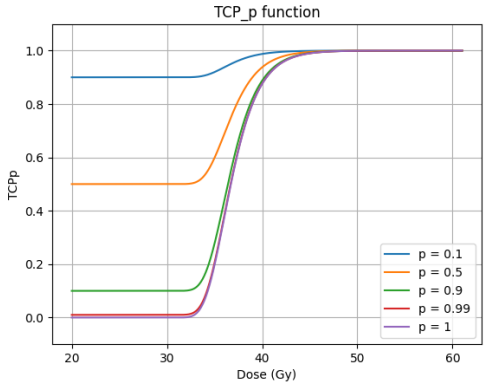

Figure 4.7: $PTCP$ (TCP_p in the figure) for different probabilities (p) of having a tumor in the voxel

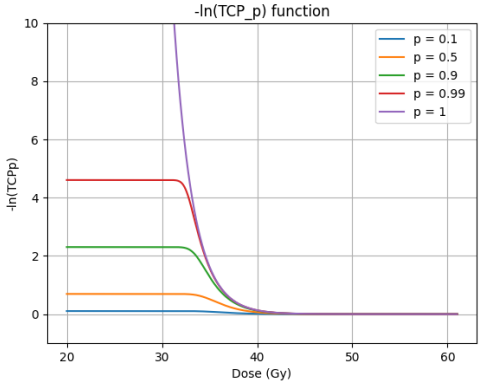

Figure 4.8: $-ln(PTCP)$ (TCP_p in the figure) for different probabilities (p) of having a tumor in the voxel

Now, if we recall:

$$\begin{aligned} & \mathcal{D} = \mathcal{B}\mathbf{x} \\ \iff \quad & d_i = \sum_j^m \mathcal{B}_{ij} \cdot x_i \ , \end{aligned} \tag{4.14}$$

with $\mathcal{B} \in \mathbb{R}^m$ the beamlet (or dose-influence) matrix for m spots.

Using the chain rule, the derivatives can be expressed as :

$$\frac{\partial}{\partial \mathbf{u}}[-ln(UTCP(\mathcal{D}))] = \frac{\partial}{\partial \mathcal{D}}[-ln(UTCP(\mathcal{D}))] \cdot \frac{\partial \mathcal{D}}{\partial \mathbf{x}} \frac{\partial \mathbf{x}}{\partial \mathbf{u}} \ . \tag{4.15}$$

So we compute the 3 derivatives :

$$\begin{aligned} \frac{\partial \mathbf{x}}{\partial \mathbf{u}} &= 2\mathbf{u} \\ \frac{\partial \mathcal{D}}{\partial \mathbf{x}} &= \mathcal{B} \ , \end{aligned} \tag{4.16}$$

and

$$\frac{\partial}{\partial \mathcal{D}}[-ln(UTCP(\mathcal{D}))] = \frac{\partial}{\partial \mathcal{D}}[-ln(PTCP(\mathcal{D}))] - \frac{\partial}{\partial \mathcal{D}}[1 - ln(NTCP(\mathcal{D}))] \ . \tag{4.17}$$

First, let us compute:

$$\begin{aligned}\frac{\partial TCP_i(d_i)}{\partial d_i} &= \frac{\partial}{\partial d_i}[e^{-\eta e^{-\alpha d_i-\beta d_i^2/n}}] \\ &= e^{-\eta e^{-\alpha d_i-\beta d_i^2/n}} \cdot \eta e^{-\alpha d_i-\beta d_i^2/n} \cdot (\alpha + \frac{2\beta}{n} d_i) \\ &= \eta(\alpha + \frac{2\beta}{n} d_i) \cdot TCP_i(d_i) \cdot SF_i(d_i) \ ,\end{aligned} \tag{4.18}$$

where we used the equations 2.3 and 3.34.
Then :

$$\begin{aligned}\frac{\partial}{\partial \mathcal{D}}(-ln(PTCP(\mathcal{D}))) &= \frac{\partial}{\partial \mathcal{D}}[-w_t \sum_{i=1}^{N_t} ln((1-p_i) + p_i TCP_i(d_i))] \\ &= -w_t \sum_{i=1}^{N_t} \frac{\partial}{\partial d_i}[ln((1-p_i) + p_i TCP_i(d_i))] \\ &= -w_t \sum_{i=1}^{N_t} \frac{p_i}{(1-p_i) + p_i TCP_i(d_i)} \frac{\partial}{\partial d_i}[TCP_i(d_i)] \\ &= -w_t \sum_{i=1}^{N_t} \eta(\alpha + \frac{2\beta}{n} d_i) \cdot SF_i(d_i) \frac{p_i TCP_i(d_i)}{(1-p_i) + p_i TCP_i(d_i)} \ ,\end{aligned} \tag{4.19}$$

and

$$\begin{aligned}-\frac{\partial}{\partial \mathcal{D}}[1 - ln(NTCP(\mathcal{D}))] &= \frac{\partial}{\partial \mathcal{D}}[-\sum_{j=1}^{S} \xi_j w_j \sum_{i=1}^{N_j} ln(1 - TCP_i(d_i))] \\ &= -\sum_{j=1}^{S} \xi_j w_j \sum_{i=1}^{N_j} \frac{\partial}{\partial d_i}[ln(1 - TCP_i(d_i))] \\ &= -\sum_{j=1}^{S} \xi_j w_j \sum_{i=1}^{N_j} \frac{1}{1 - TCP_i(d_i)} \frac{\partial}{\partial d_i}[-TCP_i(d_i)] \\ &= \sum_{j=1}^{S} \xi_j w_j \sum_{i=1}^{N_j} \eta(\alpha + \frac{2\beta}{n} d_i) \cdot SF_i(d_i) \frac{TCP_i(d_i)}{1 - TCP_i(d_i)} \ .\end{aligned} \tag{4.20}$$

Finally :

$$\begin{aligned}-\frac{\partial ln(UTCP(\mathcal{D}))}{\partial \mathcal{D}} &= \sum_{j=1}^{S} \xi_j w_j \sum_{i=1}^{N_j} \frac{\eta(\alpha + \frac{2\beta}{n} d_i) \cdot SF_i(d_i) \cdot TCP_i(d_i)}{1 - TCP_i(d_i)} \\ &\quad - w_t \sum_{i=1}^{N_t} \frac{\eta(\alpha + \frac{2\beta}{n} d_i) \cdot SF_i(d_i) \cdot p_i TCP_i(d_i)}{(1-p_i) + p_i TCP_i(d_i)} \ .\end{aligned} \tag{4.21}$$

We can notice that the gradient for $PTCP$ will be negative and the $NTCP$ gradient positive.

Combining all derivatives, we get:

$$-\frac{\partial ln(UTCP(\mathcal{D}))}{\partial \mathbf{u}} = 2 \cdot \mathcal{B} \cdot \mathbf{u} \cdot (\sum_{j=1}^{S} \xi_j w_j \sum_{i=1}^{N_j} \frac{\eta(\alpha + \frac{2\beta}{n} d_i) \cdot SF_i(d_i) \cdot TCP_i(d_i)}{1 - TCP_i(d_i)} - w_t \sum_{i=1}^{N_t} \frac{\eta(\alpha + \frac{2\beta}{n} d_i) \cdot SF_i(d_i) \cdot p_i TCP_i(d_i)}{(1 - p_i) + p_i TCP_i(d_i)}) \quad . \quad (4.22)$$

4.2.3 Optimization parameters

To compare the results of our probabilistic TCP/NTCP optimization with the current techniques that are clinically used, we performed optimization on the same CT. As UTCP optimization does not have a dose prescription, we used an equivalence between the classical parameters and the radiobiological parameters as explained in Section 3.4.2 to determine the dose constraints. The structure weights for optimization were determined in each case to obtain the best results possible, thus they are not the same between optimization. Finally, for the radiobiological parameters, we tried to remain consistent with the values in the literature [28, 44] and we kept c.

Moreover, in determining the optimal number of beams, we observed that while increasing the number of beams improves the NTCP, it also significantly extends the optimization time. We ultimately chose to use four beams, as this is standard clinical practice for this type of cancer and offers a good balance between efficiency and optimization time. The beam angles were set at 60°, 120°, 240° and 300° the gantry angles and the beam angles at 10°, 10°, 350° and 350° to replicate the treatment plan used in [75].

	UTCP			Classical	
Structure name	α	$\frac{\alpha}{\beta}$	η	Dmax	Dmin
Target (CTD/CTV)	0.4	10	$2 \cdot 10^4$	72	68
Parotid_L	0.4	3	$2 \cdot 10^4$	25	/
Parotid_R	0.4	3	$2 \cdot 10^4$	25	/
spinalCord	0.4	3	$2 \cdot 10^4$	15	/
smg_L	0.4	3	$2 \cdot 10^4$	25	/
smg_R	0.4	3	$2 \cdot 10^4$	25	/
pharConsMid	0.4	3	$2 \cdot 10^4$	20	/
BODY	0.2	8	$2 \cdot 10^4$	30	/

Table 4.1: Summary of the different ROI and parameters in both UTCP and classical optimization. Note that BODY structure is only used for optimization and not for evaluation.

Chapter 5

Results

For the conventional optimization, we used the IMPT optimizer from the OpenTPS package. The parameters used are those presented in Section 4.2.3. For probabilistic optimization, we implemented the IMPT optimizer with the cost functions for probabilistic target definition 3.25 and 3.26 for the CTD. As mentioned above, we dosed the CTD until $p_i <= 5\%$ (CTD95%). The CTD95% and the CTV are set to be the same volumes. For radiobiological optimization and probabilistic radiobiological optimization, we used the UTCP and PTUCP models described above. Because PUTCP with $p_i = 1$ is the same as UTCP, we simply reused the same derivatives and defined the probability accordingly. For both probabilistic optimizations, we used the DEVH definition to compute the dose distribution of the CTD95% (in dashed lines). The results are shown in tables 5.1, 5.2, 5.3 and 5.4. The D5 and D95 in the tables correspond to the 5% and 95% bins of the DVH/DEVH.

In our model, we assumed that all OARs are arranged in series rather than in parallel. However, this assumption created challenges in optimizing and evaluating NTCP. Thus, we had to define a region corresponding to the classical PTV with a 5mm margin from the CTV where NTCP was not computed. Without this exclusion, the proximity of some OARs to the target could result in 100% NTCP, as these OARs would be impossible to spare during optimization. Since the primary objective of our optimization was to demonstrate improvements in the UTCP function, including these regions in the NTCP evaluation would consistently lead to 0% UTCP. Furthermore, calculating NTCP in areas where the goal is to eliminate cancerous cells is not meaningful.

5.1 Conventional optimization

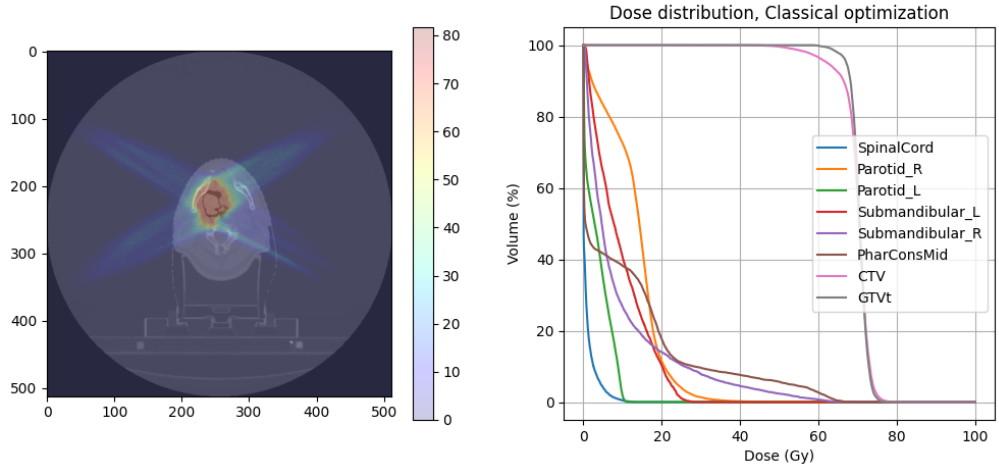

Figure 5.1: Dose image and DVH for the classical IMPT optimization, the mask displayed on the image is the GTV

Target dose	(Gy)	OAR dose	(Gy)	Radiobiological	(%)
GTV D5	73.47	Spinal cord D5	4.45	TCP	99.77
GTV D95	67.11	Parotid R D5	23.92	NTCP	100
CTV D50	69.73	Parotid L D5	9.44	UTCP	0.00
CTV D5	73.86	SMG R D5	38.07	PTCP	/
CTV D95	62.28	SMG L D5	22.29	PUTCP	/
CTV D5 - D95	11.58	PharConsMid D5	52.42		

Table 5.1: Results of the classical IMPT optimization

5.2 Probabilistic optimization

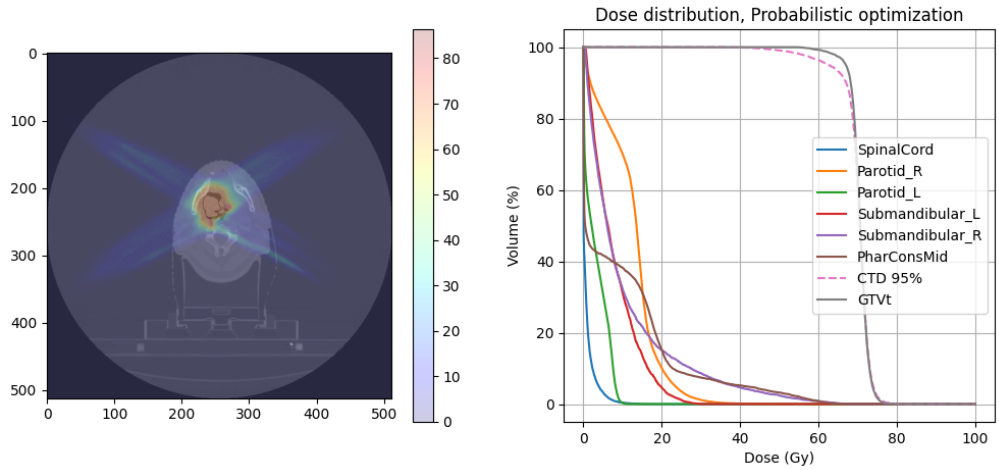

Figure 5.2: Dose image and DVH for the probabilistic optimization, the mask displayed on the image is the GTV

Target dose	(Gy)	OAR dose	(Gy)	Radiobiological	(%)
GTV D5	73.76	Spinal cord D5	3.85	TCP	39.36
GTV D95	66.97	Parotid R D5	23.46	NTCP	100
CTD(95%) D50	69.11	Parotid L D5	8.20	UTCP	0.00
CTD(95%) D5	73.97	SMG R D5	38.87	PTCP	92.06
CTD(95%) D95	62.62	SMG L D5	19.63	PUTCP	0.00
CTD(95%) D5 - D95	11.34	PharConsMid D5	41.19		

Table 5.2: Results of the probabilistic optimization

5.3 Radiobiological optimization

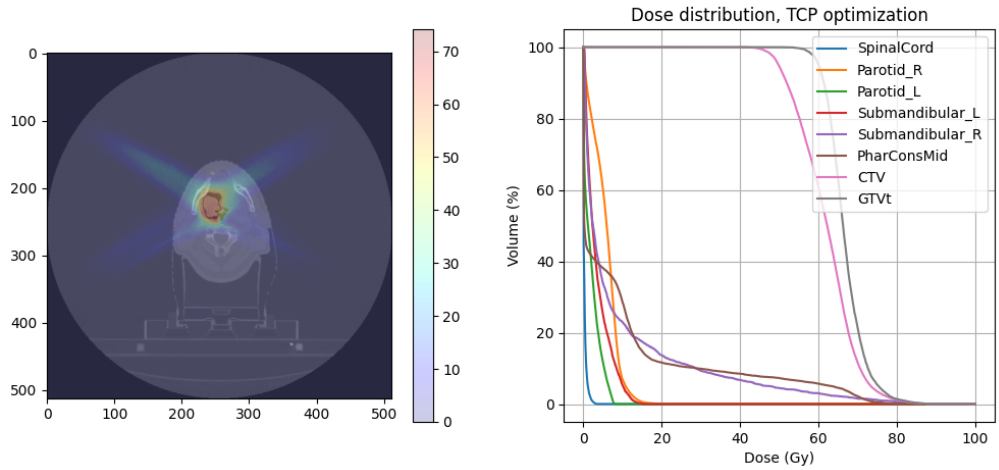

Figure 5.3: Dose image and DVH for the radiobiological optimization, the mask displayed on the image is the GTV

Target dose	(Gy)	OAR dose	(Gy)	Radiobiological	(%)
GTV D5	75.40	Spinal cord D5	1.14	TCP	98.67
GTV D95	60.01	Parotid R D5	10.77	NTCP	28.71
CTV D50	61.80	Parotid L D5	6.43	UTCP	70.33
CTV D5	73.38	SMG R D5	47.76	PTCP	/
CTV D95	49.78	SMG L D5	10.13	PUTCP	/
CTV D5 - D95	23.60	PharConsMid D5	63.41		

Table 5.3: Results of the radiobiological optimization

5.4 Probabilistic radiobiological optimization

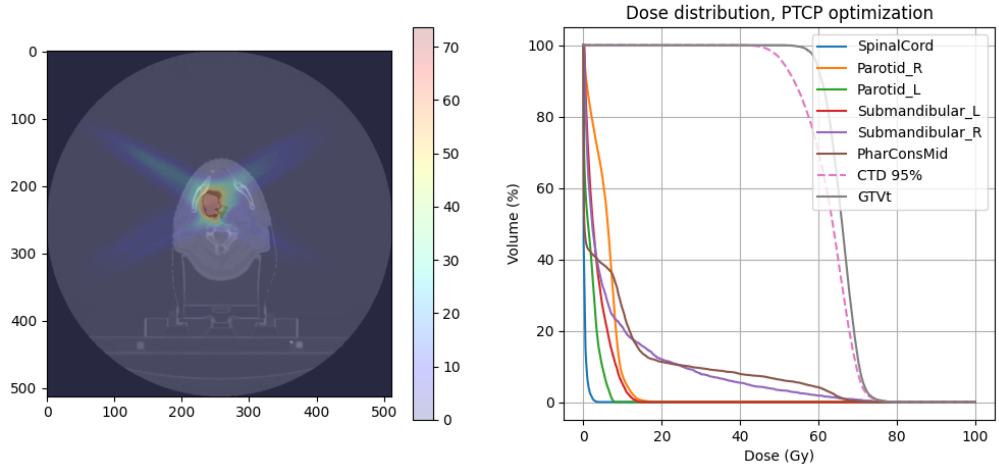

Figure 5.4: Dose image and DVH for the probabilistic radiobiological optimization, the mask displayed on the image is the GTV

Target dose	(Gy)	OAR dose	(Gy)	Radiobiological	(%)
GTV D5	71.53	Spinal cord D5	1.14	TCP	92.39
GTV D95	59.51	Parotid R D5	10.93	NTCP	4.16
CTD(95%) D50	59.44	Parotid L D5	5.93	UTCP	88.54
CTD(95%) D5	70.92	SMG R D5	41.71	PTCP	99.12
CTD(95%) D95	50.98	SMG L D5	10.01	PUTCP	94.99
CTD(95%) D5 - D95	19.94	PharConsMid D5	56.53		

Table 5.4: Results of the probabilistic radiobiological optimization

Chapter 6

Discussion

6.1 Optimization initialization

To achieve convergence in our optimization process and identify a reasonable solution (Due to non-convexity we cannot ensure that our solution is the best solution), it was crucial to provide a well-chosen initialization of the beamlets weights for the problem. Specifically, the initial weights should give a dose distribution slightly higher than the optimal dose anticipated after optimization. This approach addresses the non-convexity of the PTCP function, which can result in a zero gradient if the starting dose is too low, potentially impeding optimization. In contrast, the derivative of the NTCP function has an exponential profile, leading to excessively high gradients if the initial dose is too large. In our study, we initialized the optimizer with a prescribed dose of 100 Gy, while the expected dose after optimization was approximately 70 Gy. This initialization helped balance the gradients and guided the optimization process towards a more accurate solution.

6.2 Results evaluation

During the evaluation process, which was consistent across all optimizations, we chose not to calculate the NTCP within a 5mm margin surrounding the CTV/CTD 95%. This decision was made because it allowed us to better differentiate between NTCP outcomes across different optimizations. Without this adjustment, the NTCP values would have been nearly 100%, since the OAR is located very close to the GTV. Consequently, even a small number of voxels with high $NTCP_i$ can drive the overall NTCP score to 100%, leading to a poor UTCP result making meaningful comparisons difficult.

For the analysis of TCP or NTCP, the D95 or D5 metrics are not relevant. Indeed, if a single voxel in the target is not dosed, the total TCP is 0 (and the opposite for NTCP, if one voxel received too much dose, NTCP is 1) while the D95 (D5) could be considered good. Therefore, we will rely on the EUD (equation 3.52). Due to the equivalence of the equations 3.51 and 3.52 we can also construct an ε_f based on the NTCP similar to ζ_f (the generalization of ζ_{50} but for any percentage f). We will now define :

$$\begin{aligned} &EUD_{\zeta,f} \text{ s.t. } TCP(\mathcal{D}) = TCP(EUD_{\zeta,f}) = f \ , \\ &EUD_{\varepsilon,f} \text{ s.t. } NTCP(\mathcal{D}) = NTCP(EUD_{\varepsilon,f}) = f \ , \end{aligned} \tag{6.1}$$

with :

$$\begin{aligned} \zeta_f &:= ln(\frac{-ln(f)}{\eta N}) \ , \\ \varepsilon_f &:= ln(\frac{-ln(1-(1-f)^{1/N})}{\eta}) \ , \end{aligned} \tag{6.2}$$

and :

$$\begin{aligned} EUD_{\zeta,f} &:= -\frac{1}{2}\frac{\alpha}{\beta} n[1 - \sqrt{1 - \frac{4\beta}{\alpha^2 n}\zeta_f}] \ , \\ EUD_{\varepsilon,f} &:= -\frac{1}{2}\frac{\alpha}{\beta} n[1 - \sqrt{1 - \frac{4\beta}{\alpha^2 n}\varepsilon_f}] \ . \end{aligned} \tag{6.3}$$

Reworking our Figure 6.1, we can show the difference of $EUD_{\zeta,f}$ and $EUD_{\varepsilon,f}$ for $f = 50\%$. We can clearly see in Figure 6.1 that the effects of the dose become constant for NTCP at a certain ratio $\frac{\alpha}{\beta}$ due to the seriality of the model 3.38.

Those two formulas allow us to calculate the dose that will produce a 95% TCP in the target and the dose in the OARs that will produce a 5% NTCP as :

$$\begin{aligned} EUD_{\zeta,95} &\approx 46.97 \ Gy \ , \\ EUD_{\varepsilon,5} &\approx 15.80 \pm 0.10 \ Gy \ . \end{aligned} \tag{6.4}$$

For OARs, we did not consider the body for $EUD_{\varepsilon,5}$ evaluation as it encompasses a too-large volume. For the other OARs, the $EUD_{\varepsilon,5}$ remained more or less constant, showing that the $EUD_{\varepsilon,5}$ formula does not depend much on the volume considered.

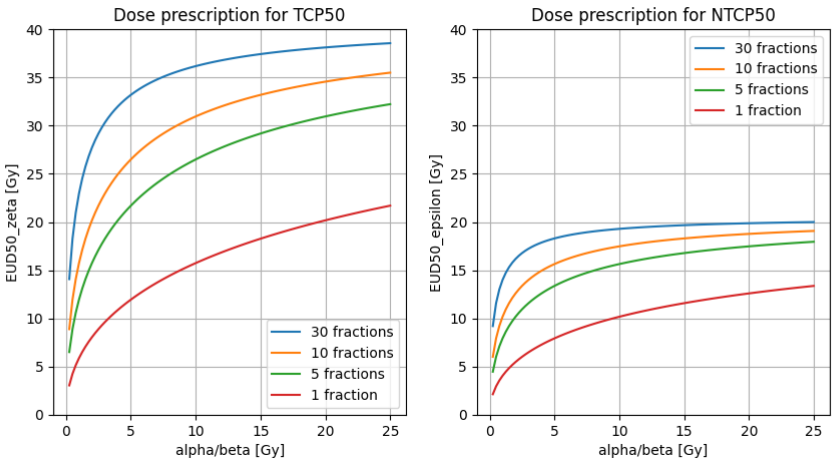

Figure 6.1: EUD_{50} depending on the ratio $\frac{\alpha}{\beta}$ (for $\alpha = 0.35[Gy]^{-1}$). The volume is $100mm^3$ and $N_0 = 10^7 cm^{-3} \cdot 100mm^3 = 10^6$.

6.3 Analysis

Let us start our analysis with some consideration to the D5 of the different OARs and the dose given to the target for each optimization.

Radiobiological optimization results in a lower D95 within the target compared to classical and probabilistic optimization. In the radiobiological model, the dose delivered to the target is minimized while ensuring that each voxel receives a sufficient dose from a radiobiological perspective. This means that not all voxels are required to receive the same dose, allowing more flexibility in dose distribution even within the target.

For the OARs, we observe an overall lower dose in the probabilistic cases. This is attributed to the CTD, which allows for better OAR sparing by reducing the high-dose regions. Furthermore, radiobiological methods tend to spare OARs that are farther from the target, while delivering higher doses to those closer to the target. This can be explained because the radiological optimization prioritizes sufficient TCP.

Regarding the radiobiological criterion, we observed very good TCP/PTCP values in both classical and probabilistic optimizations. However, their NTCP was excessively high (100%), resulting in a UTCP of 0%. This outcome was anticipated, as the main objective of these optimizers is to deliver the prescribed dose to the

target for effective treatment without considering radiobiological aspects. Although the doses to the OARs are minimized as much as possible, the close proximity between the target and some OARs is not adequately managed by these optimization methods and even if the D5 of some OAR is lower than the ones obtained with radiobiological optimization, the NTCP is higher due to few voxels with high NTCP.

In contrast, radiobiological optimization converges to a solution with an acceptable TCP and a relatively low NTCP, resulting in a significantly better overall UTCP. This improvement is even more pronounced with probabilistic optimization, which is more effective in sparing the OARs, even when they are in close proximity to the target.

However, it remains challenging to establish a definitive comparison between all the methods. As mentioned above, the most effective evaluation to compare TCP and NTCP can be performed through EUD. However, this metric is highly dependent on the radiobiological modeling and the specific parameters chosen. The EUD models developed in 6.3 are useful to compute the 5% and 95% limits but in an optimal plan, with those metrics being close to 1% and 99%, the definition 6.2 tends to $-\infty$ and $+\infty$, therefore we are forced to rely on the definition 3.52 of EUD based on the SF. As this definition is equivalent for TCP, it is not the case for NTCP because of the seriality of the organs. Yet, the SF-based EUD remains the most accessible and adapted tool to compare plans based on radiobiological criteria.

When comparing the different optimization methods, the radiobiological-based methods (UTCP and PUTCP) significantly reduce the dose delivered to the OARs (Figure 6.2), especially for the OAR close to the target (Parotid_R and Sumbandibular_L). Although we also notice that the EUD is lower with UTCP than with PUTCP, we must remind the reader that EUD based on SF is not a serial model, thus the correct NTCP is still lower for PUTCP optimization (4. 16%) than for UTCP optimization (28. 16%) (Tables 5.3 and 5.4).

To analyze target coverage, we must restrict our investigation to the GTV due to the non-probabilistic nature of the EUD. The SF based EUD and the $EUD_{\zeta,95}$ are equivalent definitions but the use of the SF based EUD allows us to avoid the infinities that would appear in the computation of ζ because the TCP is 99% for the GTV in the tree optimization methods. Radiological optimizations tend to deliver a lower dose in the GTV because the TCP condition is met. This emphasizes that radiobiological optimization focuses on achieving tumor eradication rather than respecting a dose prescription.

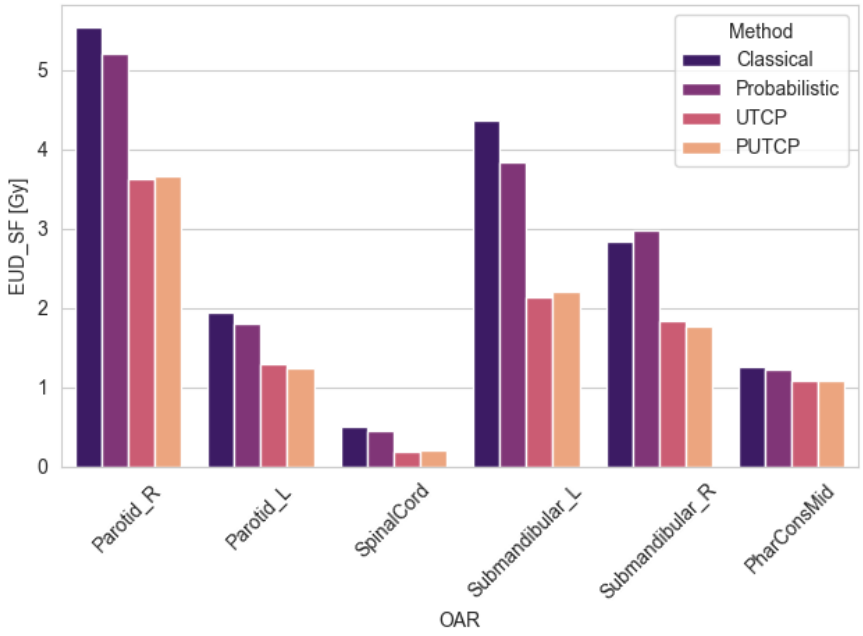

Figure 6.2: The EUD SF-based of the considered OARs (recorrected to exclude the region of 10mm arround the target). The EUD is computed with equation 3.52. The EUD is considered for the different optimization schemes.

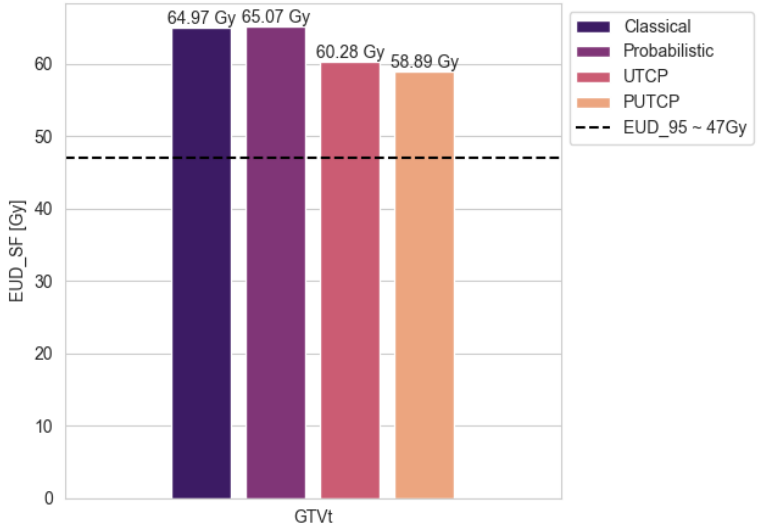

Figure 6.3: The EUD SF-based of the GTV equation (equation 3.52). The dotted line is the $EUD_{\zeta,95}$.

Chapter 7

Conclusion

7.1 Contributions

Our work demonstrated that probabilistic radiobiological optimizations are feasible, despite some limitations. Unlike classical optimizations, radiobiological optimizations are significantly more influenced by the geometry of the patient and the specific biological model used. Due to their multiplicative nature (or log-addition after convexification), radiobiological cost functions are much more punitive for deviation of the dose needed to achieve optimal tumor control or radiotoxicity to the OARs than conventional or probabilistic cost functions. This effect will render the optimization gradient rough and the gradient will vary enormously from one iteration to another; therefore, to converge, the optimization must start at a good initialization (preferably at high doses). The weight implemented in the cost functions 4.2, 4.5, served to guide the optimization process to acceptable solutions (the final evaluation being performed without the weights). However, due to the non-convex nature of the PTCP function [17], we cannot affirm that the solutions found are optimal and that optimization is not stuck into a local minimum.

In radiobiological optimization, the spatiality of the cost function is preserved until the last step (multiplication), and all the geometric mean-style approach (equations 3.34, 3.38), instead of the arithmetic mean for conventional optimization (equations 2.19, 2.20), ensures that no compromise that would leave a voxel insufficiently/too much irradiated is possible.

Because of the stronger spatial dependence of radiobiological optimizations, these methods are tailored to proton therapy. Indeed, the nature of proton beams (*i.e.*, Bragg peaks, Figure 2.1) allows one to spare OARs, thereby improving NTCP. Therefore, using a radiobiological method that encompasses NTCP is more coherent

for proton therapy than for conventional radiation therapy, where the beams pass "through and through" (Figure 2.2).

We hypothesize that beam and couch angles need to be chosen carefully to avoid OARs with small volumes and that these angles will have a significant impact on the optimization process. This is due to the fact that optimizations based on UTCP or PTCP do not allow one to "sacrifice" volumes, unlike the heuristic method proposed by Bortfeld *et al.* [17].

Compared to non-probabilistic optimizations, probabilistic optimizations, whether radiobiological or classical, allow for better OARs sparing [44]. This is due to the lower dose that is delivered to the CTV (or its equivalent, the CTD). Therefore, a better result can be achieved with respect to NTCP. Because the radiobiological models used in this master thesis are based on the SF (equation 2.3) that treats radiation damage as a stochastic process, it makes sense to treat tumor infiltration also as a stochastic or probabilistic process.

7.2 Limitations

More precise knowledge of radiobiology and better models could improve the precision and reliability of such optimization. For the purpose of our work, we tried to remain consistent with the literature and clinical practice, but it is nearly impossible to know if the model is realistic. For instance, better evaluation of the radiosensitivity for each organ could lead to greater precision.

Another area of improvement is the implementation of robust scenarios. To fully exploit the benefits of CTD and the probabilistic optimizer, it would be advantageous to develop plans that incorporate robustness against error scenarios. These scenarios would account for variability in probability distributions compared to traditional planning. In doing so, we could optimize the plan to further improve OAR sparing, taking full advantage of the probabilistic optimizer to manage uncertainties and improve overall outcomes.

The use of a PTCP model derived for independent voxel to optimize a CTD with dependent voxel is one of the weakest points of the results presented here. However, optimizing with this PTCP model favors local tumor control over total tumor control. This approach resembles the heuristic strategy presented in Bortfeld *et al.* of sacrificing subvolumes [17]. Thus, it remains a valid approach, at least for optimizations.

For evaluation, the two models are more or less equivalent for high doses [17] (Figure C.2) and when using both methods for evaluations, we did not observe any differences of more than 7% difference for probabilistic radiobiological optimizations.

The CTD model used in our work could be further improved. Currently, the dilation is isotropic and does not account for potential OARs or natural barriers that can limit tumor spread. Incorporating these factors into the CTD model could lead to more accurate results. Furthermore, the probability of tumor presence in a voxel, based on its distance from the GTV edge, is currently calculated using a 1D Gaussian distribution. A more precise approach would be to use a 3D Gaussian distribution centered on the GTV edge points, which offers a more accurate representation of tumor spread. As mentioned in [44], one solution would be to have a dedicated algorithm to inform the definition of CTD and estimate the probability of tumor presence.

As discussed previously, the non-convex nature of our PUTCP objective function complicates the achievement of optimal results. Although optimization is possible with careful initialization, the quality of the result cannot be fully guaranteed. A major limitation of our model is its inability to differentiate between parallel and serial organs for NTCP computation due to mathematical difficulties in calculating objective functions and gradients. Consequently, we treat all organs as serials, which is the more conservative approach. Developing a realistic approximation that distinguishes parallel from serial organs would lead to more accurate and radiobiologically relevant results, as it would eliminate some of the approximations we had to make to enable logarithms and derivatives in the optimization process.

7.3 Perspectives

The assumption of dependent or independent voxels can drastically change the optimization process. As models might be adapted to prevent vanishing or exploding gradients of the cost function, there are still clinical studies needed to investigate which assumption prevails [17]. In this master thesis, the CTD is defined with a Gaussian distribution. Although this approximation reflects the population-wise propagation of tumors [43], a more complex model of tumor propagation considering the anatomy surrounding the tumor (like described in Bortfeld *et al.* [78]) could be more accurate regarding the evolution of the tumor.

In broader terms, any uncertainty about tumor volume, whether due to its delineation or position, could be quantified on a probabilistic map [79, 80] and could be implemented in a fully probabilistic treatment planning framework [65].

Those uncertainties could even be rescaled by using Bayesian probabilities between treatment fractions [81].

One of the limitations of this master thesis is the lack of existing metrics to evaluate radiobiological treatments. DVHs that are commonly used in clinical practices only provide volumetric information and partial information about the dose distribution [42], and even more, they are not adapted for probabilistic evaluations. Resorting to the use of DEVH could be a solution to reflect the probabilistic nature of probabilistic planning [44], but it is still inefficient for evaluating the dose distribution with respect to radiobiological metrics. Although EUD might encompass radiobiological effects of the dose distribution [72, 73], it is still inefficient for a probabilistic dose distribution. The development of a probabilistic EUD (PEUD) might answer the need to compare treatments optimized through probabilistic radiobiological optimization.

As mentioned above, radiobiological optimization is deeply impacted by the geometry of OARs that surround the target, but optimization with a small spacing between spots for PBS is highly resource-intensive. Artificially downsizing the size of the CT to find suboptimal solutions and using those solutions as starting points for the optimization of CT resolutions approaching the true CT resolution might ensure that the gradients do not deviate from the path to the optimal solution while reducing the computation time. This idea of downsizing the image and then upsizing resembles the architecture of U-Net convolutional networks [82]. Indeed convolutional neural networks rely on spatial associativity of data [83], therefore, we hypothesize that such networks could be trained on clinical data to predict the dose distribution (that is accessible in the solution space) that results in the best UTCP/PTUCP score. The method of inverse planning could then be used to find optimal weights that mimic this dose distribution.

As mentioned in Section 2.7.1, the RBE of protons has been considered as a constant factor 1.1. However, clinical evidence shows that this assumption is not true [25]. Using a radiobiological model of SF (equation 2.3) to reflect the biological effect should also reflect this not constant RBE. Indeed, an optimization cannot be considered fully radiobiological if all the biological effects of radiation are not taken into account.

As described in Section 4.2.3, we observed an improvement in our results, primarily through a reduction in NTCP, as the number of beams increased. Emerging technologies such as ArcPT [84], which delivers beams while rotating around the patient, could offer a promising solution. ArcPT has already shown a reduction

in toxicity risk compared to conventional optimizations. Therefore, we believe that coupling radiobiological optimization with ArcPT could further enhance patient treatment by better sparing OARs (thus reducing NTCP) while maintaining sufficient TCP.

7.4 Answer to the research question

The purpose of this master thesis was to explore the computational and clinical added value of probabilistic planning. With respect to computational added value, we have shown that although classical probabilistic models have already proven their usability [16, 65, 17, 44], probabilistic radiobiological models are also feasible and provide a new insight into the solution space (Figure 3.7). Those solutions also resulted in an improved probability of tumor control and a decreased probability of normal tissue complications, granting more clinically relevant treatments, thus demonstrating the clinical added value of probabilistic radiobiological optimizations.

Even though the answers to those research questions have been obtained through several approximations (to the PTCP and NTCP models) that could deem the answer as partial, we hope that this first dive into probabilistic radiobiological optimizations could foster more research in the domain.

Appendix A

Phantom

During the development of our model and testing the feasibility of our optimization process, we used a phantom to speed up the computation time. Despite the simplified set up, we were able to obtain results that were easier to interpret and analyze. This process allowed us to understand how our optimizer functions and to identify the differences it could achieve compared to classical optimization.

To illustrate our findings, we present the results of probabilistic radiobiological optimization in Figure A.1 and probabilistic optimization in Figure A.2. The simpler geometry of the phantom and the greater distance between the OAR and the GTV compared to the real case allowed us to achieve some results (Table A.1).

Furthermore, we could also analyze the dose distribution in the GTV. Contrary to classic optimization, the dose distribution is higher in the center of the GTV and decreases as it approaches the edge to achieve the highest dose possible in the GTV (Figure A.3).

	Radiobiological	Probabilistic
TCP (%)	100	100
PTCP (%)	100	100
NTCP (%)	0	0
UTCP (%)	100	100
PUTCP (%)	100	100

Table A.1: Tumor control probabilities for PUTCP and probabilistic optimizations in phantom

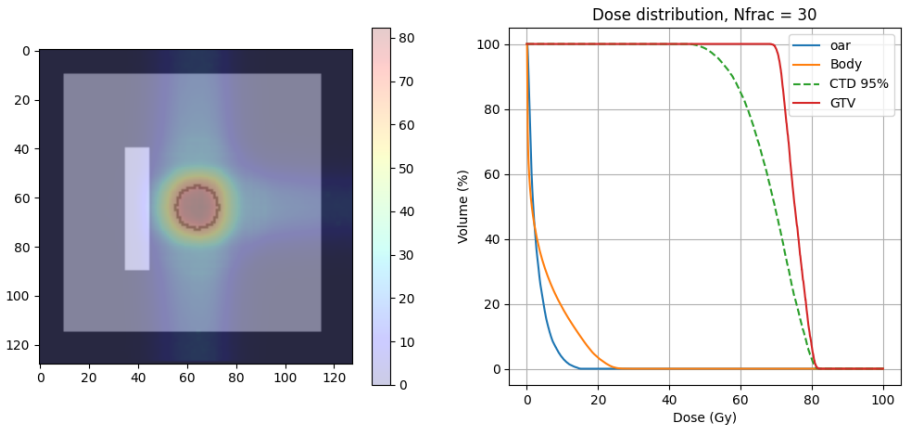

Figure A.1: Dose image and DEVH obtained after PUTCP optimization in the phantom

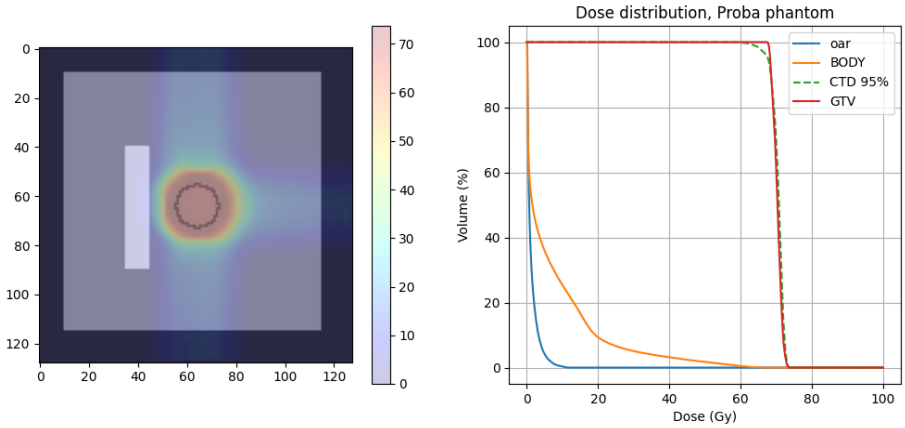

Figure A.2: Dose image and DEVH obtained after probabilistic optimization in the phantom

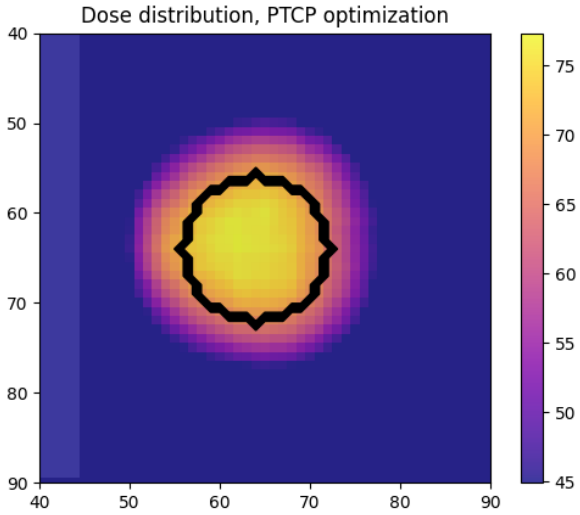

Figure A.3: Dose distribution (in Gy) on the target with the GTV contour displayed in black

Appendix B

Supplementary Figures

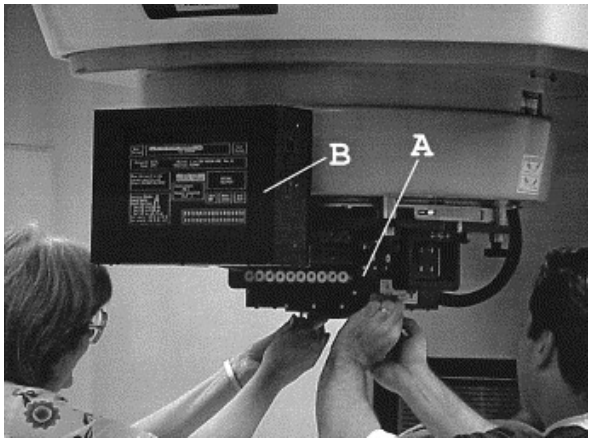

Figure B.1: The Nomos Peacock (full system) attached to a linac. (A) MIMIC MLC. (B) Controller. [85]

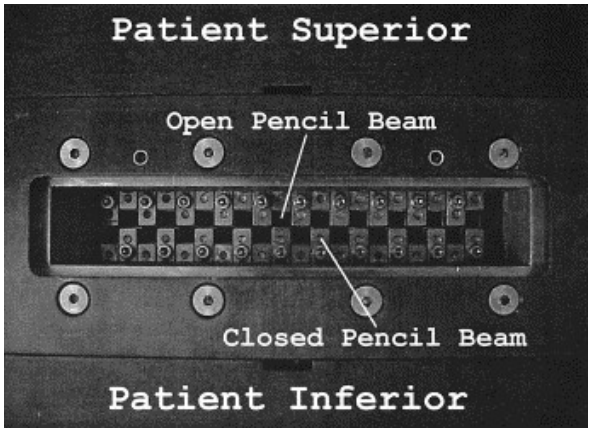

Figure B.2: Inside view of Nomos MIMIC MLC [85]

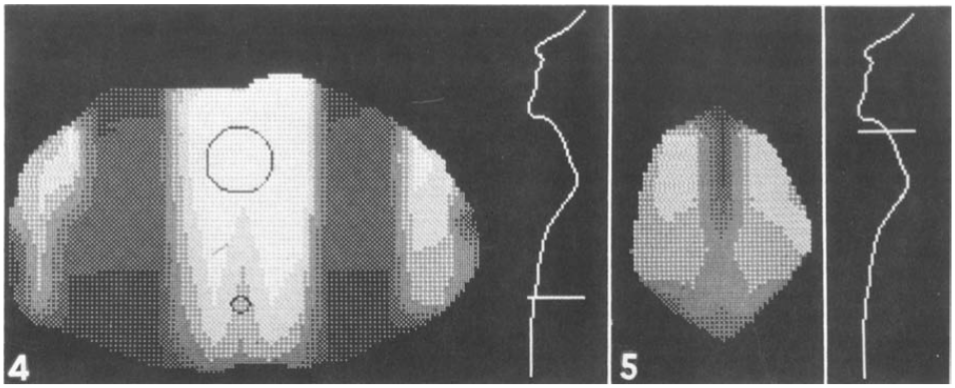

Figure B.3: Images produced by the first 3D TPS [23]

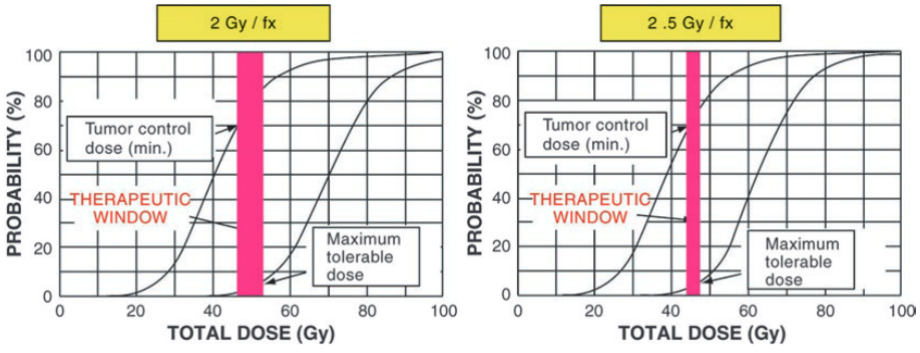

Figure B.4: Therapeutic window depending on the dose per fraction [10].

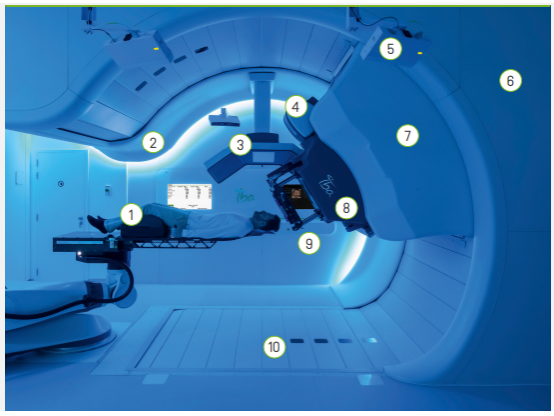

Figure B.5: The ProteusONE gantry. The nozzle is (8). [41]

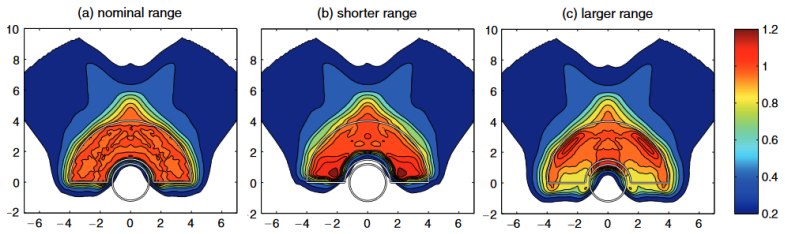

Figure B.6: Minimum, nominal and maximum range with 3 beams and $\sigma_j = 5mm$, adapted from [56] (OAR is the circle in the center and the half disk is the target).

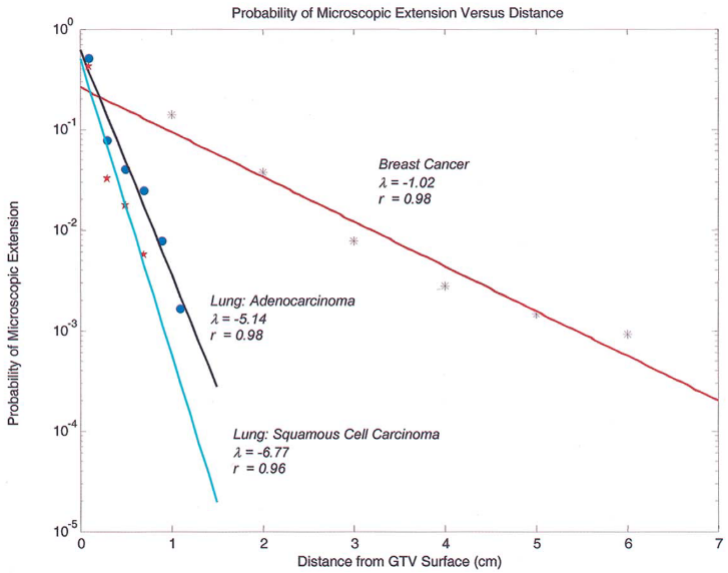

Figure B.7: Probability of finding clonogenic cells versus distance to GTV of different tumor types [62].

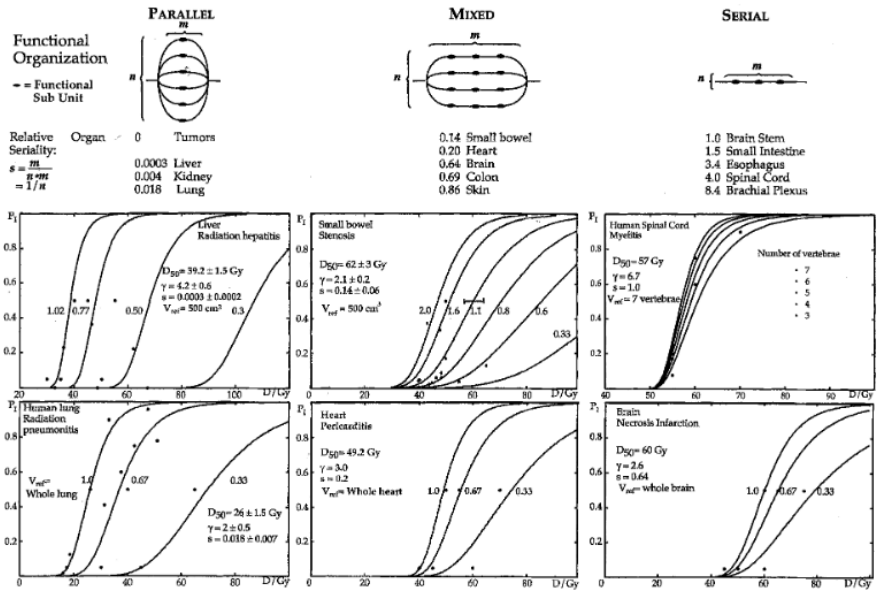

Figure B.8: NTCP curves depending on organ seriality and dose [68]

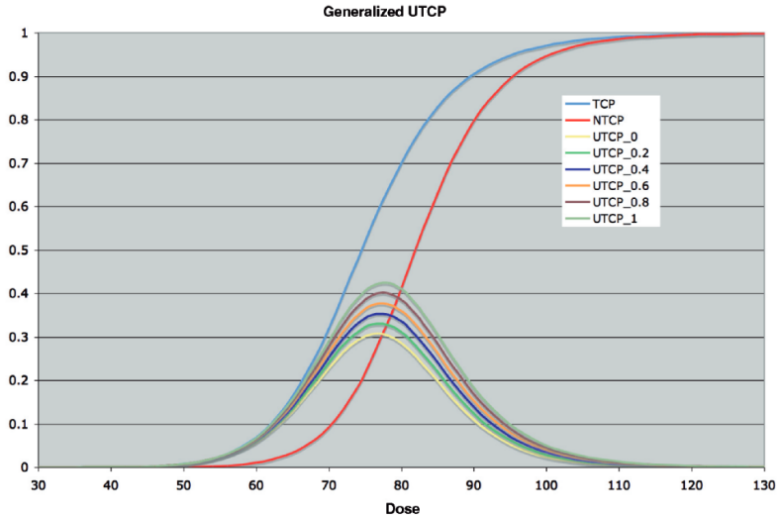

Figure B.9: Effect of the δ parameter on equation 3.46 [67]

Appendix C

Supplementary Materials

Organ name	Structure name
Tumor	Target (CTD)
Left parotid	Parotid_L
Right parotid	Parotid_R
Spinal cord	spinalCord
Left submandibular gland	smg_L
Right submandibular gland	smg_R
Middle pharyngeal constrictor muscle	pharConsMid
body	BODY

Table C.1: Summary of the different ROI used for optimization

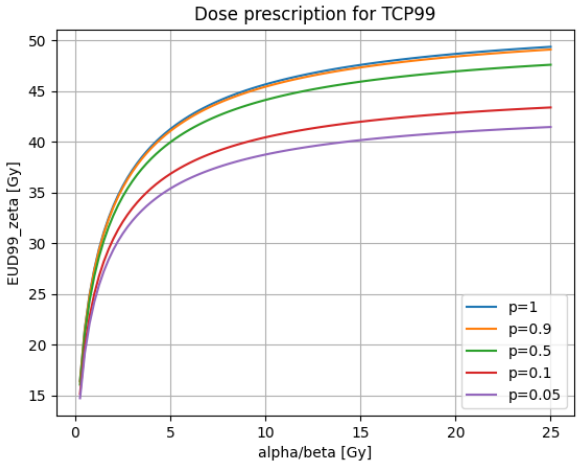

Figure C.1: $EUD_{\zeta,99}$ depending on the ratio $\frac{\alpha}{\beta}$ (for $\alpha = 0.35[Gy]^{-1}$) and the probability p_i. The volume is $100mm^3$ and $N_0 = 10^7 cm^{-3} \cdot 100mm^3 = 10^6$ and the number of fractions is 30.

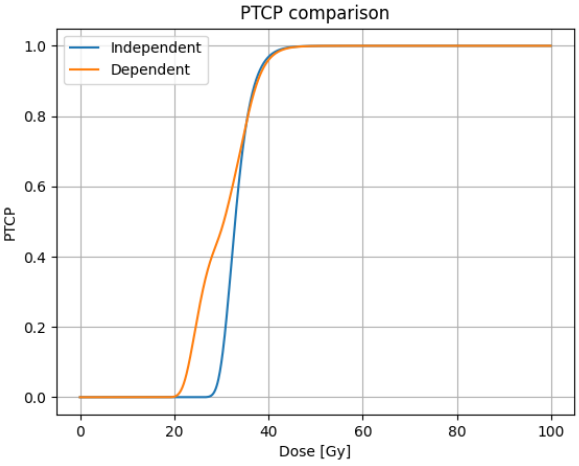

Figure C.2: Comparison of the PTCP for independent and dependent voxels model. The target is a $5\times5\times5$ cube. l_0 is $1\times1\times1$ at the center, l_1 is the $3\times3\times3$ expansion with $p_1 = 0.5$, l_2 is $5\times5\times5$ with $p_2 = 0.2$ and $p_3 = 0$. At a certain threshold (high dose), the two PTCP (equations 3.55 and 3.57) models are equivalent. The dose is uniform to the whole target.

Bibliography

[1] Janssens Guillaume, Lee John, and Sterpin Edmond, "LGBIO2070 : Engineering challenges in protontherapy."

[2] Lee John and Sterpin Edmond, "LPHMD2357 : Computational and Numerical Methods for Medical Physics."

[3] Sterpin Edmond, "WRDTH3120 : Fundamental of dosimetry."

[4] ——, "WRDTH3160 : Technology, Dosimetry and Treatment Planning in Radiotherapy."

[5] "The Cancer Atlas (website)." [Online]. Available: http://canceratlas.cancer.org/9WS

[6] C. Allen, S. Her, and D. A. Jaffray, "Radiotherapy for Cancer: Present and Future," *Advanced Drug Delivery Reviews*, vol. 109, pp. 1–2, Jan. 2017. [Online]. Available: https://linkinghub.elsevier.com/retrieve/pii/S0169409X17300133

[7] R. Mohan, "A review of proton therapy – Current status and future directions," *Precision Radiation Oncology*, vol. 6, no. 2, pp. 164–176, Jun. 2022. [Online]. Available: https://onlinelibrary.wiley.com/doi/10.1002/pro6.1149

[8] M. Beyzadeoglu, G. Ozyigit, and C. Ebruli, "Clinical Radiation Oncology," in *Basic Radiation Oncology*. Cham: Springer International Publishing, 2022, pp. 99–122. [Online]. Available: https://link.springer.com/10.1007/978-3-030-87308-0_3

[9] M. Schwarz, "Treatment planning in proton therapy," *The European Physical Journal Plus*, vol. 126, no. 7, p. 67, Jul. 2011. [Online]. Available: http://link.springer.com/10.1140/epjp/i2011-11067-y

[10] M. Beyzadeoglu, G. Ozyigit, and C. Ebruli, "Radiobiology," in *Basic Radiation Oncology*. Cham: Springer International Publishing, 2022, pp. 47–97. [Online]. Available: https://link.springer.com/10.1007/978-3-030-87308-0_2

[11] T. R. Munro and C. W. Gilbert, "The Relation Between Tumour Lethal Doses and the Radiosensitivity of Tumour Cells," *The British Journal of Radiology*, vol. 34, no. 400, pp. 246–251, Apr. 1961. [Online]. Available: https://academic.oup.com/bjr/article/34/400/246-251/7301778

[12] P. Källman, A. Ågren, and A. Brahme, "Tumour and Normal Tissue Responses to Fractionated Non-uniform Dose Delivery," *International Journal of Radiation Biology*, vol. 62, no. 2, pp. 249–262, Jan. 1992. [Online]. Available: http://www.tandfonline.com/doi/full/10.1080/09553009214552071

[13] A. L. Hoffmann, D. Den Hertog, A. Y. D. Siem, J. H. A. M. Kaanders, and H. Huizenga, "Convex reformulation of biologically-based multi-criteria intensity-modulated radiation therapy optimization including fractionation effects," *Physics in Medicine and Biology*, vol. 53, no. 22, pp. 6345–6362, Nov. 2008. [Online]. Available: https://iopscience.iop.org/article/10.1088/0031-9155/53/22/006

[14] Y. Kim and W. A. Tomé, "Risk-adaptive optimization: Selective boosting of high-risk tumor subvolumes," *International Journal of Radiation Oncology*Biology*Physics*, vol. 66, no. 5, pp. 1528–1542, Dec. 2006. [Online]. Available: https://linkinghub.elsevier.com/retrieve/pii/S0360301606027933

[15] "The International Commission on Radiation Units and Measurements," *Journal of the ICRU*, vol. 10, no. 1, pp. NP.2–NP, Apr. 2010. [Online]. Available: https://academic.oup.com/jicru/article-lookup/doi/10.1093/jicru/ndq001

[16] N. Shusharina, D. Craft, Y.-L. Chen, H. Shih, and T. Bortfeld, "The clinical target distribution: a probabilistic alternative to the clinical target volume," *Physics in Medicine & Biology*, vol. 63, no. 15, p. 155001, Jul. 2018. [Online]. Available: https://iopscience.iop.org/article/10.1088/1361-6560/aacfb4

[17] T. Bortfeld, N. Shusharina, and D. Craft, "Probabilistic definition of the clinical target volume—implications for tumor control probability modeling and optimization," *Physics in Medicine & Biology*, vol. 66, no. 1, p. 01NT01, Jan. 2021. [Online]. Available: https://iopscience.iop.org/article/10.1088/1361-6560/abcad8

[18] D. Kardamakis, S. Baatout, M. Bourguignon, N. Foray, and Y. Socol, "History of Radiation Biology," in *Radiobiology Textbook*, S. Baatout, Ed. Cham: Springer International Publishing, 2023, pp. 1–24. [Online]. Available: https://link.springer.com/10.1007/978-3-031-18810-7_1

[19] H. D. Huh and S. Kim, "History of Radiation Therapy Technology," *Progress in Medical Physics*, vol. 31, no. 3, pp. 124–134, Sep. 2020. [Online].

Available: http://www.progmedphys.org/journal/view.html?doi=10.14316/pmp.2020.31.3.124

[20] J. M. Slater, "From X-Rays to Ion Beams: A Short History of Radiation Therapy," in *Ion Beam Therapy*, U. Linz, Ed. Berlin, Heidelberg: Springer Berlin Heidelberg, 2012, vol. 320, pp. 3–16. [Online]. Available: https://link.springer.com/10.1007/978-3-642-21414-1_1

[21] A Brahme, J -E Roos, and I Lax, "Solution of an integral equation encountered in rotation therapy," *Physics in Medicine & Biology*, vol. 27, no. 10, pp. 1221–1229, Oct. 1982. [Online]. Available: https://iopscience.iop.org/article/10.1088/0031-9155/27/10/002

[22] J. A. Purdy, "3-D Radiation Treatment Planning: A New Era," in *Frontiers of Radiation Therapy and Oncology*, J. Meyer and J. Purdy, Eds. S. Karger AG, Apr. 1996, vol. 29, pp. 1–16. [Online]. Available: https://karger.com/books/book/2232/chapter/5717808

[23] T. D. Sterling, K. C. Knowlton, J. J. Weinkam, and D. M. Sterling, "Dynamic Display of Radiotherapy Plans Using Computer-Produced Films," *Radiology*, vol. 107, no. 3, pp. 689–691, Jun. 1973. [Online]. Available: http://pubs.rsna.org/doi/10.1148/107.3.689

[24] R. R. Wilson, "Radiological Use of Fast Protons," *Radiology*, vol. 47, no. 5, pp. 487–491, Nov. 1946. [Online]. Available: http://pubs.rsna.org/doi/10.1148/47.5.487

[25] R. Mohan and D. Grosshans, "Proton therapy – Present and future," *Advanced Drug Delivery Reviews*, vol. 109, pp. 26–44, Jan. 2017. [Online]. Available: https://linkinghub.elsevier.com/retrieve/pii/S0169409X16303192

[26] "What is Proton Therapy ?" [Online]. Available: http://www.iba-protontherapy.com/what-is-proton-therapy

[27] P. Andreo, D. T. Burns, A. E. Nahum, J. Seuntjens, and F. H. Attix, *Fundamentals of ionizing radiation dosimetry. Textbook / Pedro Andreo, David T. Burns, Alan E. Nahum, Jan Seuntjens, and Frank H. Attix.* Weinheim: Wiley-VCH, 2017.

[28] P. Sminia, O. Guipaud, K. Viktorsson, V. Ahire, S. Baatout, T. Boterberg, J. Cizkova, M. Dostál, C. Fernandez-Palomo, A. Filipova, A. François, M. Geiger, A. Hunter, H. Jassim, N. F. J. Edin, K. Jordan, I. Koniarová, V. K. Selvaraj, A. D. Meade, F. Milliat, A. Montoro, C. Politis, D. Savu, A. Sémont, A. Tichy, V. Válek, and G. Vogin, "Clinical Radiobiology for

Radiation Oncology," in *Radiobiology Textbook*, S. Baatout, Ed. Cham: Springer International Publishing, 2023, pp. 237–309. [Online]. Available: https://link.springer.com/10.1007/978-3-031-18810-7_5

[29] G. Schettino, S. Baatout, F. Caramelo, F. Da Pieve, C. Fernandez-Palomo, N. F. J. Edin, A. D. Meade, Y. Perrot, J. Reindl, and C. Villagrasa, "Mechanistic, Modeling, and Dosimetric Radiation Biology," in *Radiobiology Textbook*, S. Baatout, Ed. Cham: Springer International Publishing, 2023, pp. 191–236. [Online]. Available: https://doi.org/10.1007/978-3-031-18810-7_4

[30] "The Beam: Protons for head and neck cancers, a look at our RTTs, meet Angelle Schilling | Fred Hutchinson Cancer Center." [Online]. Available: https://www.fredhutch.org/en/news/blog/2024/03/the-beam-protons-for-head-and-neck-cancers-a-look-at-our-rtts-meet-angelle-schilling.html#head&neck

[31] W. D. Newhauser and R. Zhang, "The physics of proton therapy," *Physics in Medicine and Biology*, vol. 60, no. 8, pp. R155–R209, Apr. 2015. [Online]. Available: https://iopscience.iop.org/article/10.1088/0031-9155/60/8/R155

[32] J. Gueulette, R. Gahbauer, D. T. L. Jones, J. Slabbert, and A. Wambersie, "The Impact of Radiation Quality on Cure Rate," in *Ion Beam Therapy*, U. Linz, Ed. Berlin, Heidelberg: Springer Berlin Heidelberg, 2012, vol. 320, pp. 81–93, series Title: Biological and Medical Physics, Biomedical Engineering. [Online]. Available: https://link.springer.com/10.1007/978-3-642-21414-1_6

[33] D. T. Goodhead, "Radiation effects in living cells," *Canadian Journal of Physics*, vol. 68, no. 9, pp. 872–886, Sep. 1990. [Online]. Available: http://www.nrcresearchpress.com/doi/10.1139/p90-125

[34] U. Linz, "Physical and Biological Rationale for Using Ions in Therapy," in *Ion Beam Therapy*, U. Linz, Ed. Berlin, Heidelberg: Springer Berlin Heidelberg, 2012, vol. 320, pp. 45–59. [Online]. Available: https://link.springer.com/10.1007/978-3-642-21414-1_4

[35] M. Fippel and M. Soukup, "A Monte Carlo dose calculation algorithm for proton therapy," *Medical Physics*, vol. 31, no. 8, pp. 2263–2273, Jul. 2004. [Online]. Available: http://doi.wiley.com/10.1118/1.1769631

[36] K. Parodi, "Monte Carlo Methods for Dose Calculations," in *Ion Beam Therapy: Fundamentals, Technology, Clinical Applications*, U. Linz, Ed. Berlin, Heidelberg: Springer, 2012, pp. 97–116. [Online]. Available: https://doi.org/10.1007/978-3-642-21414-1_7

[37] S. F. Kry, J. Lye, C. H. Clark, N. Andratschke, A. Dimitriadis, D. Followill, R. Howell, M. Hussein, M. Ishikawa, S. Kito, T. Kron, J. Lee, J. Michalski, A. Filippo Monti, N. Reynaert, P. Taylor, K. Venables, Y. Xiao, and J. Lehmann, "Report dose-to-medium in clinical trials where available; a consensus from the Global Harmonisation Group to maximize consistency," *Radiotherapy and Oncology*, vol. 159, pp. 106–111, Jun. 2021. [Online]. Available: https://linkinghub.elsevier.com/retrieve/pii/S0167814021061326

[38] O. Jäkel, "Treatment Planning for Ion Beam Therapy," in *Ion Beam Therapy*, U. Linz, Ed. Berlin, Heidelberg: Springer Berlin Heidelberg, 2012, vol. 320, pp. 503–525, series Title: Biological and Medical Physics, Biomedical Engineering. [Online]. Available: http://link.springer.com/10.1007/978-3-642-21414-1_30

[39] X. Ding, H. Lin, J. Shen, W. Zou, K. Langen, and H.-M. Lu, "Proton Treatment Delivery Techniques," in *Target Volume Delineation and Treatment Planning for Particle Therapy*, N. Y. Lee, J. E. Leeman, O. Cahlon, K. Sine, G. Jiang, J. J. Lu, and S. Both, Eds. Cham: Springer International Publishing, 2018, pp. 17–44, series Title: Practical Guides in Radiation Oncology. [Online]. Available: http://link.springer.com/10.1007/978-3-319-42478-1_2

[40] "Centre de protonthérapie PARTICLE (website)." [Online]. Available: https://www.uzleuven.be/fr/departements-et-consultations/centre-de-protontherapie-particle

[41] IBA, "ProteusONE Brochure," 2023.

[42] J. A. Purdy, P. Poortmans, and C. A. Perez, "Three-Dimensional Treatment Planning and Conformal Therapy," in *Technical Basis of Radiation Therapy*, S. H. Levitt, J. A. Purdy, C. A. Perez, and P. Poortmans, Eds. Berlin, Heidelberg: Springer Berlin Heidelberg, 2011, pp. 253–273. [Online]. Available: https://link.springer.com/10.1007/174_2011_322

[43] S. Campbell, I. Poon, D. Markel, D. Vena, K. Higgins, D. Enepekides, S. Rapheal, J. Wong, G. Allo, E. Morgen, N. Khaoum, B. Smith, J. Balogh, R. MacKenzie, J. Davidson, D. Wang, and M. Yaffe, "Evaluation of Microscopic Disease in Oral Tongue Cancer Using Whole-Mount Histopathologic Techniques: Implications for the Management of Head-and-Neck Cancers," *International Journal of Radiation Oncology*Biology*Physics*, vol. 82, no. 2, pp. 574–581, Feb. 2012. [Online]. Available: https://linkinghub.elsevier.com/retrieve/pii/S036030161003347X

[44] G. Buti, N. Shusharina, A. Ajdari, E. Sterpin, and T. Bortfeld, "Exploring trade-offs in treatment planning for brain tumor cases

with a probabilistic definition of the clinical target volume," *Medical Physics*, vol. 50, no. 1, pp. 410–423, Jan. 2023. [Online]. Available: https://aapm.onlinelibrary.wiley.com/doi/10.1002/mp.16097

[45] E. Sterpin, A. Barragan, K. Souris, and J. Lee, "Planification de traitement robuste en protonthérapie," *Cancer/Radiothérapie*, vol. 20, no. 6-7, pp. 523–529, Oct. 2016. [Online]. Available: https://linkinghub.elsevier.com/retrieve/pii/S1278321816302323

[46] H. Paganetti, "Range uncertainties in proton therapy and the role of Monte Carlo simulations," *Physics in Medicine & Biology*, vol. 57, no. 11, p. R99, May 2012, publisher: IOP Publishing. [Online]. Available: https://dx.doi.org/10.1088/0031-9155/57/11/R99

[47] C. Möhler, T. Russ, P. Wohlfahrt, A. Elter, A. Runz, C. Richter, and S. Greilich, "Experimental verification of stopping-power prediction from single- and dual-energy computed tomography in biological tissues," *Physics in Medicine & Biology*, vol. 63, no. 2, p. 025001, Jan. 2018, publisher: IOP Publishing. [Online]. Available: https://dx.doi.org/10.1088/1361-6560/aaa1c9

[48] C. Grassberger and H. Paganetti, "Elevated LET components in clinical proton beams," *Physics in Medicine & Biology*, vol. 56, no. 20, p. 6677, Sep. 2011. [Online]. Available: https://dx.doi.org/10.1088/0031-9155/56/20/011

[49] C. Grassberger, A. Trofimov, A. Lomax, and H. Paganetti, "Variations in Linear Energy Transfer Within Clinical Proton Therapy Fields and the Potential for Biological Treatment Planning," *International Journal of Radiation Oncology*Biology*Physics*, vol. 80, no. 5, pp. 1559–1566, Aug. 2011. [Online]. Available: https://www.sciencedirect.com/science/article/pii/S0360301610034486

[50] M. Van Herk, P. Remeijer, C. Rasch, and J. V. Lebesque, "The probability of correct target dosage: dose-population histograms for deriving treatment margins in radiotherapy," *International Journal of Radiation Oncology*Biology*Physics*, vol. 47, no. 4, pp. 1121–1135, Jul. 2000. [Online]. Available: https://linkinghub.elsevier.com/retrieve/pii/S0360301600005186

[51] J.-J. Sonke, M. Aznar, and C. Rasch, "Adaptive Radiotherapy for Anatomical Changes," *Seminars in Radiation Oncology*, vol. 29, no. 3, pp. 245–257, Jul. 2019. [Online]. Available: https://www.sciencedirect.com/science/article/pii/S1053429619300165

[52] M. van Herk, "Errors and margins in radiotherapy," *Seminars in Radiation Oncology*, vol. 14, no. 1, pp. 52–64, Jan. 2004. [Online]. Available: https://www.sciencedirect.com/science/article/pii/S1053429603000845

[53] S. Wuyckens, D. Dasnoy, G. Janssens, V. Hamaide, M. Huet, E. Loÿen, G. R. de Hertaing, B. Macq, E. Sterpin, J. A. Lee, K. Souris, and S. Deffet, "OpenTPS – Open-source treatment planning system for research in proton therapy," Mar. 2023, arXiv:2303.00365 [physics]. [Online]. Available: http://arxiv.org/abs/2303.00365

[54] A. M. Barragán Montero, K. Souris, D. Sanchez-Parcerisa, E. Sterpin, and J. A. Lee, "Performance of a hybrid Monte Carlo-Pencil Beam dose algorithm for proton therapy inverse planning," *Medical Physics*, vol. 45, no. 2, pp. 846–862, Feb. 2018. [Online]. Available: https://aapm.onlinelibrary.wiley.com/doi/10.1002/mp.12688

[55] S. E. McGowan, N. G. Burnet, and A. J. Lomax, "Treatment planning optimisation in proton therapy," *The British Journal of Radiology*, vol. 86, no. 1021, pp. 20 120 288–20 120 288, Jan. 2013. [Online]. Available: https://academic.oup.com/bjr/article/86/1021/20120288/7490919

[56] J. Unkelbach, T. C. Y. Chan, and T. Bortfeld, "Accounting for range uncertainties in the optimization of intensity modulated proton therapy," *Physics in Medicine and Biology*, vol. 52, no. 10, pp. 2755–2773, May 2007. [Online]. Available: https://iopscience.iop.org/article/10.1088/0031-9155/52/10/009

[57] D. Pflugfelder, J. J. Wilkens, and U. Oelfke, "Worst case optimization: a method to account for uncertainties in the optimization of intensity modulated proton therapy," *Physics in Medicine and Biology*, vol. 53, no. 6, pp. 1689–1700, Mar. 2008. [Online]. Available: https://iopscience.iop.org/article/10.1088/0031-9155/53/6/013

[58] A. Fredriksson, "A characterization of robust radiation therapy treatment planning methods—from expected value to worst case optimization," *Medical Physics*, vol. 39, no. 8, pp. 5169–5181, Aug. 2012. [Online]. Available: https://aapm.onlinelibrary.wiley.com/doi/10.1118/1.4737113

[59] S. J. Thomas, "Margins for treatment planning of proton therapy," *Physics in Medicine and Biology*, vol. 51, no. 6, pp. 1491–1501, Mar. 2006. [Online]. Available: https://iopscience.iop.org/article/10.1088/0031-9155/51/6/009

[60] F. Albertini, E. B. Hug, and A. J. Lomax, "Is it necessary to plan with safety margins for actively scanned proton therapy?" *Physics in Medicine*

and Biology, vol. 56, no. 14, pp. 4399–4413, Jul. 2011. [Online]. Available: https://iopscience.iop.org/article/10.1088/0031-9155/56/14/011

[61] C. Njeh, "Tumor delineation: The weakest link in the search for accuracy in radiotherapy," *Journal of Medical Physics*, vol. 33, no. 4, p. 136, 2008. [Online]. Available: https://journals.lww.com/10.4103/0971-6203.44472

[62] K. Chao, A. I. Blanco, and J. F. Dempsey, "A conceptual model integrating spatial information to assess target volume coverage for IMRT treatment planning," *International Journal of Radiation Oncology*Biology*Physics*, vol. 56, no. 5, pp. 1438–1449, Aug. 2003. [Online]. Available: https://linkinghub.elsevier.com/retrieve/pii/S0360301603004292

[63] V. T. Taasti, J. Jeong, A. Jackson, and J. O. Deasy, "A theoretical investigation of adequate range uncertainty margins in proton treatment planning to preserve tumor control probability," *Acta Oncologica*, vol. 58, no. 10, pp. 1446–1450, Oct. 2019. [Online]. Available: https://www.tandfonline.com/doi/full/10.1080/0284186X.2019.1627415

[64] J. Dutreix, M. Tubiana, and A. Dutreix, "An approach to the interpretation of clinical data on the tumour control probability-dose relationship," *Radiotherapy and Oncology*, vol. 11, no. 3, pp. 239–248, Mar. 1988. [Online]. Available: https://linkinghub.elsevier.com/retrieve/pii/0167814088900060

[65] G. Buti, K. Souris, A. Maria Barragán Montero, J. Aldo Lee, and E. Sterpin, "Introducing a probabilistic definition of the target in a robust treatment planning framework," *Physics in Medicine & Biology*, vol. 66, no. 15, p. 155008, Aug. 2021. [Online]. Available: https://iopscience.iop.org/article/10.1088/1361-6560/ac1265

[66] A. Niemierko, "Biological Optimization," in *Image-Guided IMRT*, T. Bortfeld, R. Schmidt-Ullrich, W. De Neve, and D. E. Wazer, Eds. Berlin, Heidelberg: Springer Berlin Heidelberg, 2006, pp. 199–216. [Online]. Available: http://link.springer.com/10.1007/3-540-30356-1_16

[67] S. M. Bentzen, P. M. Harari, W. A. Tomé, M. P. Mehta, and S. T. Rosen, Eds., *Radiation Oncology Advances*, ser. Cancer Treatment and Research. Boston, MA: Springer US, 2008, vol. 139. [Online]. Available: http://link.springer.com/10.1007/978-0-387-36744-6

[68] A. Brahme, "Optimized radiation therapy based on radiobiological objectives," *Seminars in Radiation Oncology*, vol. 9, no. 1, pp. 35–47, Jan. 1999. [Online]. Available: https://linkinghub.elsevier.com/retrieve/pii/S1053429699800538

[69] A. Ågren, A. Brahme, and I. Turesson, "Optimization of uncomplicated control for head and neck tumors," *International Journal of Radiation Oncology*Biology*Physics*, vol. 19, no. 4, pp. 1077–1085, Oct. 1990. [Online]. Available: https://linkinghub.elsevier.com/retrieve/pii/036030169090037K

[70] C. Schinkel, N. Stavreva, P. Stavrev, M. Carlone, and B. Fallone, "Functional form comparison between the population and the individual Poisson based TCP models," *Radiology and Oncology*, vol. 41, no. 2, Jan. 2007. [Online]. Available: https://content.sciendo.com/doi/10.2478/v10019-007-0016-7

[71] S. Webb, P. M. Evans, W. Swindell, and J. O. Deasy, "A proof that uniform dose gives the greatest TCP for fixed integral dose in the planning target volume," *Physics in Medicine and Biology*, vol. 39, no. 11, pp. 2091–2098, Nov. 1994. [Online]. Available: https://iopscience.iop.org/article/10.1088/0031-9155/39/11/018

[72] A. Niemierko, "Reporting and analyzing dose distributions: A concept of equivalent uniform dose," *Medical Physics*, vol. 24, no. 1, pp. 103–110, Jan. 1997. [Online]. Available: https://aapm.onlinelibrary.wiley.com/doi/10.1118/1.598063

[73] J. E. McGary, W. G. Iii, and S. Y. Woo, "Applying the equivalent uniform dose formulation based on the linear-quadratic model to inhomogeneous tumor dose distributions: Caution for analyzing and reporting," *Journal of Applied Clinical Medical Physics*, vol. 1, no. 4, pp. 126–137, Sep. 2000. [Online]. Available: https://aapm.onlinelibrary.wiley.com/doi/10.1120/jacmp.v1i4.2634

[74] A. M. Haghighi, A. A. Kumar, and D. P. Mishev, "Optimization," in *Higher Mathematics for Science and Engineering*, A. M. Haghighi, A. A. Kumar, and D. P. Mishev, Eds. Singapore: Springer Nature, 2024, pp. 585–625. [Online]. Available: https://doi.org/10.1007/978-981-99-5431-5_10

[75] M. Huet-Dastarac, S. Michiels, S. T. Rivas, H. Ozan, E. Sterpin, J. A. Lee, and A. Barragan-Montero, "Patient selection for proton therapy using Normal Tissue Complication Probability with deep learning dose prediction for oropharyngeal cancer," *Medical Physics*, vol. 50, no. 10, pp. 6201–6214, Oct. 2023. [Online]. Available: https://aapm.onlinelibrary.wiley.com/doi/10.1002/mp.16431

[76] B. M. Beadle and C. M. Anderson, "CTV Guidance for Head and Neck Cancers," *International Journal of Radiation Oncology*Biology*Physics*, vol. 100, no. 4, pp. 903–905, Mar. 2018. [Online]. Available: https://linkinghub.elsevier.com/retrieve/pii/S0360301617344851

[77] N. Andrei, "Quasi-Newton Methods," in *Modern Numerical Nonlinear Optimization*, N. Andrei, Ed. Cham: Springer International Publishing, 2022, pp. 261–314. [Online]. Available: https://doi.org/10.1007/978-3-031-08720-2_6

[78] T. Bortfeld and G. Buti, "Modeling the propagation of tumor fronts with shortest path and diffusion models—implications for the definition of the clinical target volume," *Physics in Medicine & Biology*, vol. 67, no. 15, p. 155014, Aug. 2022. [Online]. Available: https://iopscience.iop.org/article/10.1088/1361-6560/ac8043

[79] L. Rivetti, A. Studen, M. Sharma, J. Chan, and R. Jeraj, "Uncertainty estimation and evaluation of deformation image registration based convolutional neural networks," *Physics in Medicine & Biology*, vol. 69, no. 11, p. 115045, May 2024, publisher: IOP Publishing. [Online]. Available: https://dx.doi.org/10.1088/1361-6560/ad4c4f

[80] A. Smolders, L. Rivetti, N. Vatterodt, S. Korreman, A. Lomax, M. Sharma, A. Studen, D. C. Weber, R. Jeraj, and F. Albetini, "DiffuseRT: predicting likely anatomical deformations of patients undergoing radiotherapy," *Physics in Medicine & Biology*, vol. 69, no. 15, p. 155016, Aug. 2024. [Online]. Available: https://iopscience.iop.org/article/10.1088/1361-6560/ad61b7

[81] R. Labarbe, G. Janssens, and E. Sterpin, "Estimating patient specific uncertainty parameters for adaptive treatment re-planning in proton therapy using *in vivo* range measurements and Bayesian inference: application to setup and stopping power errors," *Physics in Medicine and Biology*, vol. 61, no. 17, pp. 6281–6296, Sep. 2016. [Online]. Available: https://iopscience.iop.org/article/10.1088/0031-9155/61/17/6281

[82] M. Krithika alias AnbuDevi and K. Suganthi, "Review of Semantic Segmentation of Medical Images Using Modified Architectures of UNET," *Diagnostics*, vol. 12, no. 12, p. 3064, Dec. 2022, number: 12 Publisher: Multidisciplinary Digital Publishing Institute. [Online]. Available: https://www.mdpi.com/2075-4418/12/12/3064

[83] Y. LeCun, Y. Bengio, and G. Hinton, "Deep learning," *Nature*, vol. 521, no. 7553, pp. 436–444, May 2015. [Online]. Available: https://www.nature.com/articles/nature14539

[84] B. A. De Jong, E. W. Korevaar, A. Maring, C. I. Werkman, D. Scandurra, G. Janssens, S. Both, and J. A. Langendijk, "Proton arc therapy increases the benefit of proton therapy for oropharyngeal cancer patients in the model based

clinic," *Radiotherapy and Oncology*, vol. 184, p. 109670, Jul. 2023. [Online]. Available: https://linkinghub.elsevier.com/retrieve/pii/S0167814023002086

[85] B. J. Salter, "Nomos Peacock IMRT utilizing the BEAK™ post collimation device," *Medical Dosimetry*, vol. 26, no. 1, pp. 37–45, Mar. 2001. [Online]. Available: https://www.sciencedirect.com/science/article/pii/S0958394700000625

UNIVERSITÉ CATHOLIQUE DE LOUVAIN
École polytechnique de Louvain
Rue Archimède, 1 bte L6.11.01, 1348 Louvain-la-Neuve, Belgique | **www.uclouvain.be/epl**